

# **SANDIA REPORT**

SAND2005-3210  
Unlimited Release  
Printed June 2005

## **Validation of a Simple Turbulence Model Suitable for Closure of Temporally- Filtered Navier-Stokes Equations Using a Helium Plume**

Sheldon R. Tieszen, Stefan P. Domino, Amalia R. Black

Prepared by  
Sandia National Laboratories  
Albuquerque, New Mexico 87185 and Livermore, California 94550

Approved for public release; further dissemination unlimited.



Issued by Sandia National Laboratories, operated for the United States Department of Energy by Sandia Corporation.

**NOTICE:** This report was prepared as an account of work sponsored by an agency of the United States Government. Neither the United States Government, nor any agency thereof, nor any of their employees, nor any of their contractors, subcontractors, or their employees, make any warranty, express or implied, or assume any legal liability or responsibility for the accuracy, completeness, or usefulness of any information, apparatus, product, or process disclosed, or represent that its use would not infringe privately owned rights. Reference herein to any specific commercial product, process, or service by trade name, trademark, manufacturer, or otherwise, does not necessarily constitute or imply its endorsement, recommendation, or favoring by the United States Government, any agency thereof, or any of their contractors or subcontractors. The views and opinions expressed herein do not necessarily state or reflect those of the United States Government, any agency thereof, or any of their contractors.

Printed in the United States of America. This report has been reproduced directly from the best available copy.

Available to DOE and DOE contractors from

U.S. Department of Energy  
Office of Scientific and Technical Information  
P.O. Box 62  
Oak Ridge, TN 37831

Telephone: (865)576-8401  
Facsimile: (865)576-5728  
E-Mail: [reports@adonis.osti.gov](mailto:reports@adonis.osti.gov)  
Online ordering: <http://www.osti.gov/bridge>

Available to the public from

U.S. Department of Commerce  
National Technical Information Service  
5285 Port Royal Rd  
Springfield, VA 22161

Telephone: (800)553-6847  
Facsimile: (703)605-6900  
E-Mail: [orders@ntis.fedworld.gov](mailto:orders@ntis.fedworld.gov)  
Online order: <http://www.ntis.gov/help/ordermethods.asp?loc=7-4-0#online>



# **Validation of a Simple Turbulence Model Suitable for Closure of Temporally-Filtered Navier-Stokes Equations Using a Helium Plume**

Sheldon R. Tieszen, Stefan P. Domino, and Amalia R. Black  
Sandia National Laboratories  
Albuquerque, New Mexico 87185

## **Abstract**

A validation study has been conducted for a turbulence model used to close the temporally filtered Navier Stokes (TFNS) equations. A turbulence model was purposely built to support fire simulations under the Accelerated Strategic Computing (ASC) program. The model was developed so that fire transients could be simulated and it has been implemented in SIERRA/Fuego. The model is validated using helium plume data acquired for the Weapon System Certification Campaign (C6) program in the Fire Laboratory for Model Accreditation and Experiments (FLAME). The helium plume experiments were chosen as the first validation problem for SIERRA/Fuego because they embody the first pair-wise coupling of scalar and momentum fields found in fire plumes. The validation study includes solution verification through grid and time step refinement studies. A formal statistical comparison is used to assess the model uncertainty. The metric uses the centerline vertical velocity of the plume. The results indicate that the simple model is within the 95% confidence interval of the data for elevations greater than 0.4 meters and is never more than twice the confidence interval from the data. The model clearly captures the dominant puffing mode in the fire but under resolves the vorticity field. Grid dependency of the model is noted.

## Acknowledgments

The author wishes to thank Dr. David Pruett, James Madison University, for his pioneering work in temporal filtering of the Navier Stokes equations, and sharing his insights with us. The turbulence model developed in this report was developed at Sandia National Laboratories through the ASC Program, in the Material and Physics Models subprogram in support of abnormal thermal (fire) environments. The authors would like to thank Justine Johannes of Sandia for her support of the model development. The data used for validation in this report was obtained at Sandia National Laboratories through the Weapon Systems Engineering Certification Campaign (C6) program in support of abnormal thermal environments. The authors would like to thank Louis A. Gritzo of Sandia for his support of the data acquisition. The numerical simulation tool used in this study, SIERRA/Fuego, was developed at Sandia National Laboratories under the ASC program. The authors would like to thank Steve Kempka and Ed Boucheron, of Sandia, for their support of the development of Fuego. The ASC Verification and Validation program at Sandia National Laboratories provided funding for this validation study. The authors would like to thank Martin Pilch of Sandia for his support of this study. The quantitative validation metric used in this study was developed by Bill Oberkamp of Sandia.

Sandia is a multiprogram laboratory operated by Sandia Corporation, a Lockheed Martin Company, for the United States Department of Energy under Contract DE-AC04-94AL85000.

# Table of Contents

Nomenclature.....	7
Executive Summary.....	8
Introduction.....	10
Mathematical Model.....	15
Temporal Filtering.....	15
Closure Model.....	20
Numerical Implementation.....	26
Validation.....	29
Experimental Data Summary.....	29
Validation Simulation Matrix.....	33
Simulation Results and Data Comparisons.....	35
Quantifying the Uncertainties.....	41
Discussion.....	44
Dynamics of Buoyant Turbulence.....	44
Buoyant Vorticity Generation.....	45
Toward Effects on Heat Transfer.....	50
Conclusions.....	53
References.....	54

## List of Figures

Fig 1. Interpretation of a Temporal Filter .....	16
Fig 2. Interpretation of a Spatial Filter.....	17
Fig 3. Interpretation of the Production Term in the Turbulent Kinetic Energy Equation for TFNS.....	24
Fig 4. Sample 2D control volume definition used in the CVFEM element-based technique .....	27
Fig 5. Photograph of the Fire Laboratory for Accreditation of Models and Experiments (FLAME) .....	30
Fig 6. Schematic of the Flame Facility Showing Relationship of Plume, Laser Illumination, and Cameras.....	30
Fig 7. Favre-averaged Vertical Velocity Profile Data (m/s).....	31
Fig 8. Favre-averaged Horizontal Velocity Profile Data (m/s).....	31
Fig 9. Time-averaged Plume Density Profile Data (kg/m <sup>3</sup> ).....	32
Fig 10. Favre-averaged Turbulent Kinetic Energy Profile Estimate (m <sup>2</sup> /s <sup>2</sup> ) .....	32
Fig 11. Validation Simulation Matrix .....	33
Fig 12. Comparative Mesh Densities.....	34
Fig 13. Favre-averaged Vertical Velocity (m/s) Profiles .....	35
Fig 14. Instantaneous Density Profiles (kg/m <sup>3</sup> ) and Vertical Velocity Vectors ....	36
Fig 15. Favre-averaged Horizontal Velocity (m/s) Profiles.....	37
Fig 16. Time-averaged Density (kg/m <sup>3</sup> ) Profiles.....	37
Fig 17. Favre-averaged Turbulent Kinetic Energy (m <sup>2</sup> /s <sup>2</sup> ) Profiles.....	38
Fig 18. Comparison of Data and 2M Node Simulation Results .....	39
Fig 19. Time Step Study Profiles.....	40
Fig 20. Centerline Vertical Velocity for the Four Densities Studied.....	42
Fig 21. Centerline Vertical Velocity Data and 2M Node TFNS Simulation .....	42
Fig 22. Experimental Confidence Interval and Estimated Error of 2M TFNS Simulation.....	43
Fig 23. Model Comparison for Instantaneous Density Profiles (kg/m <sup>3</sup> ) .....	46
Fig 24. Model Comparison for Favre-averaged Vertical Velocity Profiles (m/s) .	46
Fig 25. Model Comparison for Favre-averaged Horizontal Velocity Profiles (m/s).....	47
Fig 26. Model Comparison for Time-averaged Density Profiles (kg/m <sup>3</sup> ) .....	47
Fig 27. Model Comparison for Favre-averaged Turbulent Kinetic Energy Profiles (m <sup>2</sup> /s <sup>2</sup> ).....	48
Fig 28. Temporal Filter Study Profiles .....	49
Fig 29. Two Dimensional Natural Convection Simulation for the Conditions of Evans, et al., 2004.....	51

## Nomenclature

$C$	Arbitrary constant
$f$	Arbitrary function
$g$	Gravity
$G$	Filter function kernel, for example, a Gaussian profile
$k$	Turbulent kinetic energy
$l$	Spatial filter width
$P$	Pressure
$t$	Time
$U$	Velocity
$x$	Spatial coordinate

### Greek Symbols

$\varepsilon$	Dissipation of turbulent kinetic energy
$\delta$	Kronecker delta, valid for $i = j$
$\mu$	Viscosity
$\rho$	Density
$\sigma$	Stress tensor
$\tau$	Temporal filter width

### Superscripts

$\vec{\phi}$	Vector quantity
$\phi'$	Integration variable
$\phi''$	Fluctuating quantity
$\bar{\phi}$	Time-average of quantity
$\tilde{\phi}$	Density weighted time-average (i.e., Favre-average) of quantity

### Subscripts

$\phi_{i,j}$	Directional indices
$\phi_{\infty}$	Reference value
$\phi_{k,m}$	Implied sum over all directional indices
$\phi_t$	Turbulent

## Executive Summary

This study, and a similar companion study by Nicolette, et al., 2004, are the first of several planned for the validation of the models used in the fire code SIERRA/Fuego. This study compares predictions with data from an isothermal helium plume. The only coupled physics in this problem is between the scalar field and the momentum field, and as such is the most fundamental of the planned studies. Its purpose is to evaluate the validity of the turbulence model to predict the overall plume behavior in a buoyant plume. The simple plume behavior reflects the coupling between buoyancy and turbulence that dominates turbulent mixing in a fire without the presence of combustion and soot radiation complications.

For the current study, a temporal filtering approach (referred to as Temporally Filtered Navier Stokes, TFNS) has been employed that is a compromise between the long duration (highly damping) filtering employed by pure Reynolds-Averaged Navier-Stokes (RANS) approaches and small spatial filters employed in high resolution Large Eddy Simulation (LES). Filtering the equations separates the responsibility of capturing the dynamics inherent in the equations into discretized partial differential equations and subfilter engineering models.

One of the key goals of the subfilter closure model is to bridge the gap between well-established limits. As the temporal filter width,  $\tau$ , approaches infinity, the filtered equations recover the RANS limit. As the filter width approaches zero, the equations revert to the unfiltered Navier-Stokes equations. In between these limits, an eddy viscosity closure is derived based on incorporation of the temporal filter width explicitly in the eddy viscosity definition. The resulting closure model has the physical interpretation of modeling that fraction of the production of turbulent kinetic energy spectrum that has higher frequency content than the inverse of the temporal filter.

The filtered equations and closure model are implemented in SIERRA/Fuego, a low-Mach number, turbulent reacting flow code, employing discretization on unstructured meshes using a control volume finite element method (CVFEM). The implementation of elements of the code important to the success of this validation study has been verified prior to validation.

The experimental data set used for comparison was developed at Sandia National Laboratories by the Weapons Engineering Certification Campaign explicitly for use in validating the turbulence models in SIERRA/Fuego/Syrinx. Two-dimensional velocity fields were measured using Particle Image Velocimetry (PIV). Two-dimensional distributions of the plume mass fraction were determined by seeding the plume with small amounts of acetone vapor and oxygen, and measuring Planar Laser-Induced Fluorescence (PLIF) of the acetone. Multiple repeat data sets were acquired for a single set of experimental parameters.

The simulation matrix consists of varying two numerical parameters and two model formulations. The numerical parameters include grid and time step refinements. The turbulence model is a subfilter k- $\epsilon$  model based on a temporal filter width,  $\tau_{filter}$ , with and without a term for buoyant vorticity generation. The grid refinement study shows that the model has significant grid sensitivity up to the 2M node grid used in this study in spite of the use of a constant filter width. The time-step refinement study shows relative insensitivity to time-step refinement for the medium grid employed. Qualitatively, the 2M node solution matches the data profiles for vertical and horizontal mean velocity, mean density, and turbulent kinetic energy reasonably well. Discrepancies can be attributed to the inability of the subfilter model to capture the effect of small scale vortical mixing at the base of the plume. A statistical metric is employed to quantitatively characterize the uncertainties. The results indicate that the simple model is within the 95% confidence interval of the data for elevations greater than 0.4 meters and is never more than twice the confidence interval from the data.

The model sensitivity studies indicate that a buoyant vorticity generation modification (Nicolette, et al., 2004) to the standard k- $\epsilon$  model reduces the grid dependency of the result. However, with the buoyant vorticity generation modification, the increased viscosity also results in poorer predictions of the data for a given mesh density than using TFNS with the standard k- $\epsilon$  model. It is concluded that the buoyant vorticity model developed for RANS is not extensible to TFNS because it is based on an eddy viscosity closure. A more advanced formulation would be needed to make it generally useful in TFNS. The temporal filter width study shows little effect of varying the filter width for the medium mesh density used. This result suggests that temporal and spatial discretization are not independent. The mesh must be sufficiently refined for variations in the temporal filter to show effect.

## Introduction

This study, and a similar companion study by Nicolette, et al., 2004, are the first of several planned for the validation (Tieszen, et al. 2001, Tieszen, et al. 2002, Boughton, et al., 2003) of the models used in the fire code SIERRA/Fuego. The overall goal of these studies will be to establish the uncertainty in heat flux predictions from SIERRA/Fuego/Syrinx in abnormal thermal environment applications. The goal of this study is to validate (that is to characterize the uncertainty in) a simple closure model. The model is intended for applications near the RANS limit. In fires, the slowest turbulence mode is the large-scale fluctuations that are on the order of seconds for fires larger than about 2 meters in diameter. It is desirable to develop a model that will produce results that will give the correct limiting behavior in the ergodic sense and will work reasonably well at resolving the slowest modes.

Advantages of such a model include more relevant inputs to subgrid combustion, soot formation, and effective radiative property models, and the ability to introduce into the simulation tool, virtual instrumentation models, such as thermocouples, that are based on thermal inputs that are time-resolved relative to the instruments themselves. It is well known that the turbulence is most complex at its largest scales. By resolving the largest scales, and modeling smaller scales, the turbulence models can become either simpler, or potentially more accurate, or both. The scope of this study is limited to the validation of a simple turbulence closure model for the temporally filtered Navier Stokes equation solution of an isothermal helium plume.

The overall approach to validation for SIERRA/Fuego/Syrinx can be found in Tieszen et al., 2001. This helium plume validation study is the most fundamental of the planned studies. Its purpose is to evaluate the validity of the turbulence model to predict the overall plume behavior in an isothermal buoyant plume. As noted in Tieszen, et al., 2001, fires can be classified as reacting plumes. By validating the turbulence model in a non-reacting plume, the effect of buoyancy-generated turbulence can be tested independent of the complexity introduced by turbulent combustion.

The coupling mechanism between the scalar field (species) and the momentum field is through the local density. The species composition determines the local density through the mixture molecular weight. For buoyant, low Mach-number flows, the source term in the momentum equations is the product of the difference between the local density and a reference density multiplied by gravity. Hence the local density relative to a reference density multiplied by gravity is the forcing function for a buoyant flow. This buoyant forcing results in mixing that in turn changes the local density. Thus, two sets of equations are coupled. Turbulence resulting directly from this coupling is referred to as buoyancy generated turbulence. It is postulated that the turbulence arises due to a combination of strong buoyant vorticity generation (BVG) and vorticity transport mechanisms that lead to entanglement of the vorticity resulting in a turbulent field.

As a reacting plume, the coupling mechanism between species and momentum characteristic of plumes is also present in a fire. There is also a strong coupling between energy and momentum through the change in temperature due to combustion. Combustion also affects the species distributions (and hence mixture molecular weight) and turbulence generation via a damping of vorticity generation due to dilatation. In a fire, the local density is a function of both temperature and species, the description of which involves an entire suite of fire submodels. However, to lead order, combustion generally results in temperatures and species compositions such that the products of combustion have a density that is on the order of 1/7 that of air. The density difference between the combustion products and the reactants drives not only the overall momentum, but also the turbulence. The turbulence in turn drives the combustion. The bidirectional coupling is quite strong.

For an isothermal helium plume, the density is only a function of the helium and air composition, which does not change except through the mixing induced by the momentum equations (ignoring the small effects of laminar differential diffusion). The molecular weight of helium is on the order of 1/7 of that of air, and is, therefore, a good simulant for combustion products. As with the fire, the local density gradients drive not only the overall momentum but also the turbulence. The turbulence drives the mixing which determines the local gradients. The bi-directional coupling is quite strong.

Thus, the non-reacting, isothermal plume is a simplified analog of the reacting fire, in which the most important coupling, i.e., the local density, between the species and the momentum fields is present at levels directly relevant to fire applications. The analogy is not perfect in that the density difference between plume and air decreases monotonically with elevation about the plume source, while with fires, the density difference initially increases with elevation due to dilatation, and decreases monotonically only after combustion is complete. In spite of the differences between reacting and non-reacting flows, the ability of a turbulence model to capture the lead order coupling effect can be tested in relevant conditions to fire environments without the complexity of combustion (that brings in a whole suite of models due to the length scales involved and the multiphysics nature of combustion).

As noted in Tieszen et al., 2001, abnormal thermal environment application needs drive the overall strategy for fire models. In general, heating of the internal components within objects is dominated by conduction, which is a slow process relative to convection for objects of relevance. Thus, for many applications of relevance, there is a time-scale separation between thermal response time scales of objects and fire excitation time-scales, with thermal response times being much longer. An unfortunate consequence of this separation is that fire simulations must run for long time scales, perhaps many thousands of seconds to appropriately load the objects during fire transients. In some applications, the fire will reach a quasi-steady state in tens of seconds, allowing for simplifications and in some applications, the fire will be transient over the same timescales as the thermal response, either because the flow field is being affected by the thermal response, or because boundary conditions are changing (due to material decomposition, melting, changes in the wind, fuel flow rate, etc.).

To accommodate the long simulation times required by this physics-based time-scale separation, and the vast range of length scales involved in fires (Tieszen, et al., 2001), the fundamental transport equations, (i.e., the Navier-Stokes equations) are often density weighted and temporally averaged. Specifically, they are Favre weighted and time filtered. The result is called RANS (Reynolds Average Navier-Stokes) equations or sometimes FANS (Favre-Averaged Navier-Stokes) equations. This approach is among the earliest filtering methods employed to obtain solutions to the Navier-Stokes equations. Its greatest strength is also its most significant drawback. It is based on a large filter width that permits large time steps, but results in the heaviest use of models of any filtering or averaging technique currently in use.

Filtering the equations, by whatever means, separates responsibility of capturing the dynamics inherent in the equations into that fraction to be captured by discretized partial differential equations and that fraction to be captured by subfilter engineering models. RANS is based on an ergodicity argument that assumes the mean flow is steady, or at least quasi-steady. As a result, the full turbulent energy spectrum is modeled. It cannot be overemphasized that the physics-based time-scale separation of the intended application (that results in very long simulation times) provides strong motivation to employ this strategy in spite of the heavy use of modeling.

However, many applications within the fluid mechanics community do not require these long simulation times. As such, RANS has lost favor to more recently developed filtering techniques such as spatially filtered Large Eddy Simulation (LES) approaches within the research community. The big difference between RANS and LES is not the difference between temporal and spatial filtering, but that in RANS, the filter width is maximized while in LES it is minimized. LES attempts to resolve all the scales that can be resolved up to the limit of the discretization employed. The advantages of minimizing the filter are two fold. First the amount of physics modeled vs. resolved is minimized. Second, the information being passed from the resolved scales to the subfilter models is more relevant.

Turbulence, and especially turbulent combustion, is a very non-linear process. (A complete description of the implications of this non-linearity is beyond the scope of this introduction.) As is often the case with very non-linear processes, the time-averaged output is not a direct function of the time-averaged inputs. Thus, there are limits to the accuracy of the time-averaged output of subfilter models that can be achieved with time-averaged inputs to these models.

In summary, the smaller the filter width, the more accurate the time-averaged output of the turbulence models can be theoretically. On the other hand, the smaller the filter, the higher the computational expense. For very long computational timescales (tens to hundreds of thousands of time steps) required by the fire application, LES is not practical.

Both RANS and LES techniques have been evaluated using helium plume data. The results of the RANS study are summarized in Nicolette, et al., 2004, and the LES study in DesJardin, et al., 2004. The RANS models in the Nicolette et al., 2004 study have been implemented into SIERRA/Fuego and are intended to be the primary model suite used for fire simulations. Both the standard k- $\epsilon$  turbulence model and a modification accounting for BVG were tested against the data sets to be used in the current validation study. The results indicated that the BVG modification gave superior predictions to the standard k- $\epsilon$  turbulence model for all mesh resolutions tested up to 2 M nodes. However, the results also showed that the laminar to turbulent transition was difficult to predict with this class of models, and that the laminar buoyant instability resulted in transient solutions with higher mesh densities.

The results of the LES study by DesJardin, et al., 2004 used a research code with high accuracy numerics (fourth order and higher) and mesh densities in excess of 1 M nodes as well as minimal filtering of the Navier-Stokes equations. The results were correspondingly impressive; however, even for these conditions, the simulations could not match the momentum field data for the first half plume diameter in elevation, nor the scalar field decay in the second half plume diameter in elevation. In practice, LES requires sufficient grid density that much of the energy producing and bearing scales are resolved, since LES closure models used in common practice are relative simple descriptions that assume the modeled part of the turbulent cascade is universal and dissipative.

For the current study, a filtering approach has been employed that is a compromise between the heavy filtering employed by pure RANS approaches and the high cost of high resolution LES. Choosing an intermediate approach is not a novel idea. It has been pursued by a number of investigators over the years interested in practical applications. Examples include the mixed spatial/temporal (Detached Eddy Simulation) filtering employed by Spalart and colleagues (cf., Spalart, 1999), and the partial averaging techniques of Girimaji and colleagues (cf., Girimaji, et al., 2003). The filtering technique employed here is a temporal filter (Pruett, 2000, Pruet, et al., 2003) as is RANS, but with the intended purpose of creating a narrower filter width. The model will be developed more fully in the next section. Briefly, a narrower temporal filter (referred to herein as TFNS) is used to produce a set of equations with the potential to be accurate for temporal frequencies down to tenths of seconds. In fires, this temporal resolution will permit resolution of the largest turbulent mixing structures and also allow for adequate response times for thermocouples, enabling an accurate virtual thermocouple model to be employed in the simulation for comparison with experimental data.

The application space for TFNS is somewhat counter-intuitive. Even though it has a higher temporal resolution compared to RANS, its application to fires is for those conditions in which the fire will reach a steady state in relatively short time scales. TFNS will by its nature be more expensive computationally than RANS. As a result, its applicability will be limited to scenarios where the fire reaches a quasi-steady period. For these conditions, TFNS is expected to yield a better (lower uncertainty) answer for steady state fires compared to the more heavily modeled RANS solution. For fires that have no

true steady state, because of slow transients in boundary conditions, or changes in geometry, etc., TFNS will still be too expensive to be practical. Thus, to cover the full range of fire application space, both RANS and TFNS approaches will be used.

The subject of this study is the validation of a TFNS turbulence closure model using the same helium plume data used in the Nicolette, et al., 2004 study. The model will be developed in the next section. That section will be followed by the validation section that will introduce the validation matrix, summarize the test data, present the simulation results with data comparisons, and discuss statistical validation. A discussion section follows the validation section and treats issues of subfilter models for buoyant vorticity generation and consequences to heat transfer. Conclusions will be drawn in the final section.

## Mathematical Model

To model a fire environment, conservation equations (mass, momentum, species, and energy) containing significant source terms for the effects of combustion, soot formation/destruction/transport, radiation, and buoyancy are needed for. A full specification of the conservation equations is beyond the scope of this report. However, a full description, including discretization schemes exists in the Fuego Theory Manual (available from the authors). In summary, the minimum subset for hydrocarbon pool fire simulation requires solving a variable-property, high-Grashof-number, low-Mach-number turbulent flow problem. All conservation equations must be filtered to remove physics with a higher frequency content than the intended discretization will allow. The higher frequency information is modeled. This combination prevents inappropriate aliasing (or spectral shifting from high frequency to low frequency). In the sections that follow, the momentum equations (Navier-Stokes Equations) will be filtered using a variable width temporal filter.

### Temporal Filtering

The low Mach number Navier-Stokes equations can be written in the following form.

$$\frac{\partial(\rho\vec{U})}{\partial t} + \nabla \cdot (\rho\vec{U}\vec{U}) = -\nabla P + \overline{\nabla \cdot \sigma} + (\rho - \rho_\infty)\vec{g} \quad \text{Eq. 1}$$

In the low Mach number formulation, the pressure gradient in Eq. 1 is due to fluid motion, and the density is a function of temperature and species only. The Navier-Stokes are dynamical equations and must be filtered to prevent aliasing. There are many types of filters or averaging techniques that can be employed including temporal or spatial filtering and ensemble averaging. A temporal filter with density weighting (to address variable property effects) has the following form.

$$\widetilde{f}(t) = \frac{1}{\bar{\rho}} \int_{-\infty}^t \rho(\tau) G(t, \tau) f(\tau) d\tau \quad \text{Eq. 2}$$

The function  $G$  is the parameterized filter kernel and can have a number of different forms. If the filter is to be applied explicitly as part of the solution process, as in a reconstruction method (cf., Pruett, et al., 2003), its form directly impacts the solution process. Otherwise, if the filter is applied to the equations only, the resulting parameterization is insensitive to the form of the filter kernel. The latter is the case for this study. As will be shown later, the filter will be absorbed into the closure model as a parameter. Thus for our purposes, it is sufficient to think of the filter kernel as a “top hat” filter of width  $\tau$ , i.e., its value is unity between the present time  $t$  and  $t-\tau$  and zero everywhere else.

In this form, the filter has a simple interpretation given in Fig. 1. It is simply the integral of the function over the time interval between time steps (divided by the time step). It is directly analogous to a hardware filter on a digital data acquisition system that integrates a signal between digital sampling points. Filtering the equations separates responsibility of capturing the dynamics inherent in the equations into subfilter models (analogous to a hardware filter) and discretized partial differential equations (analogous to a digital sampling system).

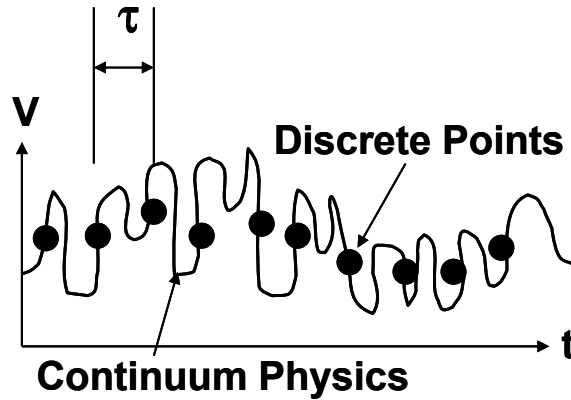


Figure 1. Interpretation of a Temporal Filter

A spatial filter with density weighting (to address variable property effects) has the following form.

$$\tilde{f}(\bar{x}) = \frac{1}{\bar{\rho}} \int_{-\infty}^{\infty} \rho(\bar{x}') G(\bar{x}, \bar{x}') f(\bar{x}') d\bar{x}' \quad \text{Eq. 3}$$

As with the temporal filter, the function  $G$  is the parameterized filter kernel and can have a number of different forms. A physical interpretation of a “top hat” spatial filter is shown in Fig. 2, for a three by three mesh scale filter. The filter is centered on each cell resulting in information overlap with adjacent filters. Spatial filters form the basis for Large Eddy Simulation (LES) and because of commutative issues, the filter function  $G$  comes in a variety of forms.

A detailed comparison of the advantages and disadvantages of the various filtering or averaging methods is beyond the scope of the present study. Pruet 2000, and Pruet, et al., 2003, are excellent sources for understanding temporal filtering and its advantages and disadvantages. Relative to the fire application, the advantages of temporal filtering include the following:

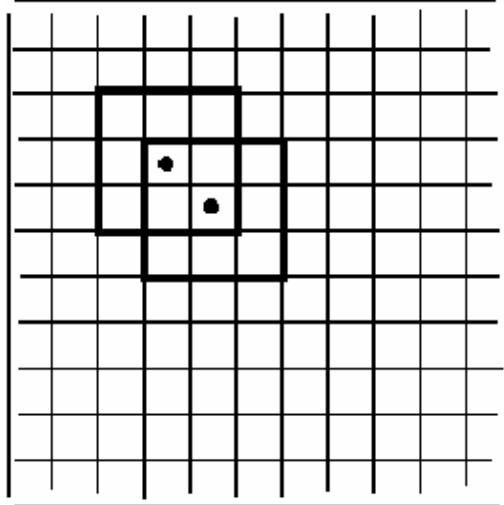


Figure 2. Interpretation of a Spatial Filter

- 1) **Compatibility of temporal filtering with Reynolds Averaging.** For fire applications, very often there is a time scale separation between turbulence time scales (advective processes) and conduction in the solid (diffusive process). Thus, heat transfer processes naturally filter in time. For thermally massive objects, the transient heating times can be very long, which favors long time averaging. The classical long time-averaged limit results in the RANS equations. For objects which are not thermally massive, and have non-linear response, such as ignition or phase change characteristics, it is valuable to have more narrowly defined temporal filtering, such that low to moderate frequency temperature and flux excursions that may result in non-linear coupling can be resolved.
- 2) **Temporal filters are normally bounded at the limits.** To obtain a filtered variable within a transport equation, it is necessary to transpose the filtering operation with differentiation. Temporal filters are normally bounded at the limits and by separation of variables; it can be shown that filtering and differentiation are commutative. The same cannot be said in general for spatial filters, particularly for unstructured, heterogeneous, anisotropic, and large expansion ratio meshes. For Department of Energy applications, these non-ideal mesh conditions will dominate applications. A substantial body of work has been done to characterize and minimize adverse effects from non-commutative operators by the LES community, but temporal filters bypass the issue.
- 3) **Allow practical separation of model and numerical errors.** As identified above, the role of a filter is to separate responsibility for managing spectral dynamical content into subfilter models and discretized solution of the resultant partial differential equations (PDEs). It is highly desirable from a validation perspective to similarly separate the error sources into subfilter models (modeling error) and PDE solution (numerical error) clearly. To accomplish this task, the mathematical equations must be independent of the mesh or time step chosen. Spatially, the filter width must not be tied to the mesh density. In theory, neither spatial nor temporal filters need be tied to either the mesh density or time step.

However, in practice, almost all LES is done with filters tied directly to the mesh density. Most practical meshes involve large expansion ratios. In areas in which it is desired to have the highest physics resolution the cells sizes are small. However, near the boundaries, where the physics is less important the mesh is large. If a single spatial filter width is chosen, it is typically inappropriately small at the boundaries, or inappropriately large in the highly resolved areas. A temporal filter on the other hand can be set to be constant for the entire mesh, because (with today's solver technology) the entire mesh is advanced uniformly in time, regardless of the size of the computational elements. As long as the time step is less than half the temporal filter width, the time step does not have to be constant with time.

- 4) **Addresses a single realization.** Both spatial and temporal filtering, as opposed to ensemble, averaging address a single realization of the physics. In safety applications, this aspect is highly desirable. With ensemble averaging approaches the outcome is known as a statistical expectation or mean. For example with ensemble averaging, one could conclude, "in the mean, the plane will not fall out of the sky." This fact is of little comfort to a passenger who is wondering if the plane he or she is personally on is going to fall out of the sky.

The disadvantages of temporal filtering include the following.

- 1) **Temporal filters are not centered filters.** Temporal filters are by necessity causal. That is they cannot integrate over future unknown events, only over past knowable events. Thus, they are "one sided" or upwind to use a spatial analogy. As noted by Pruett, 2000, for filters of the type considered here, the temporal filtering would result in phase shifting if filtering were to be employed at more than one level. In the current study, filtering will only be done at one level, so phase shifting will not be an issue. However, many of the advanced turbulence models for LES use a two level dynamic procedure. In theory, this effect of phase lag could be accounted for at the various time levels and overcome. However, it would introduce considerable complexity. At the near DNS limit, Pruett, et al., 2003 have shown that differential filters used in a reconstruction method can overcome this issue effectively. For the current application, slow diffusion controlled conduction processes imply that only low to moderate frequencies need to be resolved. Thus, the current study is an attempt to resolve dynamics in the near RANS limit as opposed to Pruett and colleagues for the near DNS limit. The phase lag issue will be most difficult in the applications between these limits.
- 2) **Galilean invariance issues.** It is important for turbulence models to honor Galilean invariance (reference frame invariance) characteristics. Issues with determining the properties that would result from temporally filtering the Navier-Stokes equations delayed the use of temporal filters. Pruett, et al., 2003 address this problem in detail. For non-inertial, non-constant reference frames, temporally filtered quantities may not be interpretable in the usual inertial context. Applications where this factor may become an issue is fires onboard military fighter aircraft undergoing rapidly varying g loads. For the current study, it is not an issue.

**3) A uniform temporal filter results in a non-uniform spatial filter (and vice versa).** The instantaneous velocity affects the spatial width of a temporal filter. Thus, in areas of high velocity, the physical length scale of the filter is larger than in areas of lower velocity. Note also that since velocity is a vector quantity, the spatial extent of a given filter will vary in coordinate directions to the extent the velocity does. Similarly, a uniform spatial filter implies a non-uniform temporal filter because of the same relation between time and space through velocity. For a constant spatial filter, the implied temporal extent of the filtering is not unique in a non-homogenous velocity field. Thus, the two filtering techniques are not identical and have different interpretations. In the limit of homogeneous, isotropic turbulence with a zero mean velocity field, it is possible to relate temporal and spatial filtering. Note that much of the fluid mechanics data available for validation has been taken at a single point in space and processed in time. This fact is not strictly true for the data set to be used in the current study as it is field data obtained through Particle Image Velocimetry.

Regardless of the type of filter employed, the Navier-Stokes equations are filtered in the same manner. The Navier-Stokes equations themselves (Eq. 1) are taken as the function to be filtered in either Eq. 2 (temporal filtering) or Eq. 3 (spatial filtering). Filtering and addition (or subtraction) are commutative. So the terms in Equation 1 can be treated as the function call in Eq. 2 or 3. For the temporal filter, because the endpoints of the integration are bounded, it can be shown through integration by parts, that differentiation and filtering can be commuted. Thus, for temporal filtering, the result is a set of temporally filtered Navier-Stokes equations (hereafter referred to as TFNS) as given in Eq. 4.

$$\frac{\partial(\overline{\rho\tilde{U}})}{\partial t} + \nabla \cdot (\overline{\rho\tilde{U}\tilde{U}}) = -\overline{\nabla P} + \overline{\nabla \cdot \sigma} + (\bar{\rho} - \bar{\rho}_\infty)\bar{g} \quad \text{Eq. 4}$$

The advective term is nonlinear and needs to be modeled. It is traditional to modify Eq. 4 so that it has more of the form of the original Navier-Stokes equations by adding a resolvable term to each side of the equation and moving the modeled term to the right hand side of the equation as shown in Eq. 5.

$$\frac{\partial(\overline{\rho\tilde{U}})}{\partial t} + \nabla \cdot (\overline{\rho\tilde{U}\tilde{U}}) = -\overline{\nabla P} + \overline{\nabla \cdot \sigma} + (\bar{\rho} - \bar{\rho}_\infty)\bar{g} + \nabla \cdot ((\overline{\rho\tilde{U}\tilde{U}}) - (\overline{\rho\tilde{U}\tilde{U}})) \quad \text{Eq. 5}$$

A closure model for the last term on the right hand side of Eq. 5 will be developed in the next section. However, since the application space of this modeling effort is in the near RANS limit, it is useful to further develop Eq. 5 under the assumptions necessary to obtain the RANS equations so that physical interpretations can be made to modeled terms as the temporal filter width is made narrower in time. The classical derivation of the RANS equations involves decomposing the velocity into the mean and fluctuating components. It is useful to do that decomposition to permit physical interpretations.

$$\bar{\rho}\vec{U} = \bar{\rho}(\vec{U} + \vec{u}'' ) \quad \text{Eq. 6}$$

The interpretation of the mean quantity in Eq. 6 is given by Eq. 2. The fluctuation is the difference between the instantaneous velocity and the mean. Substituting Eq. 6 into the Eq. 5, the modeled term becomes,

$$\nabla \cdot ((\overline{\overline{\rho\vec{U}\vec{U}}}) - (\overline{\overline{\rho\vec{U}\vec{U}}})) = -\nabla \cdot (\overline{\overline{\rho\vec{U}\vec{U}}} - \overline{\overline{\rho\vec{U}\vec{U}}} + 2\overline{\overline{\rho u''\vec{U}}} + \overline{\overline{\rho u''u''}}) \quad \text{Eq. 7}$$

If Eq. 7 were spatially filtered, the first two terms on the right hand side would be called the Leonard stresses, the third term is the cross stresses, and the final term is the Reynolds stress. The RANS equations result from simplifications to Eq. 7 based on the hypothesis (i.e., the ergodic hypothesis) that the flow is statistically stationary. If the flow is stationary, then its mean is a constant. Twice filtering of a constant is still a constant, and thus, the first and second terms in the ergodic limit are equal and cancel out. Also a consequence of the ergodic limit is that if the mean is a constant, then the time-average (density weighted in this case) of the fluctuating velocity must be zero. Thus, the cross-stress term is zero in the ergodic limit. Only the last term, i.e., the Reynolds stress term, remains to be modeled in that limit.

## Closure Model

As discussed above, filtering the equations separates responsibility of capturing the dynamics inherent in the equations into subfilter models (which are analogous to a hardware filter) and discretized partial differential equations (which are analogous to a digital sampling system). The role of the subfilter models is to capture the integral effect of the high frequency content on the lower frequency content. The equivalent mathematical statement is embodied in the last term in Eq. 5. It is the filtered or integral effect of the non-linear terms that contain high frequency components.

Eq. 5 states the requirements that a subfilter model must satisfy, but does not give any guidance as to the underlying physics that must be modeled in order to satisfy that requirement. Further, the subfilter model relies on filtered quantities as inputs. One of the strongest motivations for increasing the temporal resolution of the PDE solution is so that the subfilter models have inputs that are less heavily filtered. Being able to resolve the low frequency fluctuations will permit the development of better combustion, soot and radiation models because the information being passed from the discretized PDE's to the subfilter models is more detailed and hence, more relevant.

Turbulence, combustion and radiation are all highly non-linear processes. For non-linear processes, it is rarely the case that the mean output (as required by the modeled term in Eq. 5 for example) is solely a function of mean inputs. Thus, to the extent that the filtered equations can resolve some of the transients, the inputs to the models become increasingly relevant. A common method of supplying additional information to the subfilter models in addition to the mean quantities is to take moments of the equations so

that fluctuating information as well as mean information is passed to the subfilter models. In this context, the turbulent kinetic energy represents the sum of the one-half of the variance of the mean velocity components. For the current study, it will be employed as a means of estimating the magnitude of the turbulent fluctuations.

One of the key goals of the current modeling is to recover the RANS limit as the filter width,  $\tau$ , approaches infinity (to permit large time steps for long integration times). Of lesser importance, but desirable on a theoretical basis, is to recover the Navier-Stokes equations in the limit as the filter width,  $\tau$ , becomes vanishingly small (hereafter referred to as the Direct Numerical Simulation, DNS, limit). As noted above, in the RANS limit, all of the turbulent dynamics is modeled, while in the DNS limit, none of it is. Thus, the types of dynamics required to be captured by the subfilter model varies from only dissipation in the near DNS limit to transport, production, and dissipation in the near RANS limit. There are many RANS turbulence closure models of varying levels of fidelity, the discussion of which is beyond the scope of this report. Interested readers can find a current discussion in Durbin and Pettersson-Reif, 2001, for example.

As a pragmatic matter and for comparison to existing work, for this study a standard turbulent eddy viscosity closure model is used for the mean flow equations. In the RANS limit, the eddy viscosity will be defined in terms of a standard k- $\epsilon$  model. Thus, transport equations must be derived and solved for these quantities. Weaknesses with the standard two equation k- $\epsilon$  model are well known, particularly for flows with large coherent structures where the eddy viscosity is clearly not isotropic. It is hoped that as the largest, slowest turbulence modes become resolved rather than modeled, that a standard k- $\epsilon$  model will be the appropriate level of closure model, i.e., not requiring the anisotropy of the more complex full Reynold Stress level closures, but requiring more than just the dissipation provided by a Smagorinski model.

In the RANS limit, using the standard derivation and closure assumptions, and switching to Einsteinian notation for convenience, the last term in Eq. 7 is modeled as

$$-\rho \widetilde{u_i'' u_j''} = \mu_t \left( \frac{\partial \widetilde{U}_i}{\partial x_j} + \frac{\partial \widetilde{U}_j}{\partial x_i} - \frac{2}{3} \frac{\partial \widetilde{U}_k}{\partial x_k} \delta_{ij} \right) - \frac{2}{3} \widetilde{\rho k} \delta_{ij} \quad \text{Eq. 8}$$

where

$$\mu_t = C_\mu \widetilde{\rho} \frac{\widetilde{k}^2}{\widetilde{\epsilon}} = C_\mu \widetilde{\rho k} \left( \frac{\widetilde{k}}{\widetilde{\epsilon}} \right) \quad \text{Eq. 9}$$

and

$$\begin{aligned}
\frac{\partial(\bar{\rho}\tilde{k})}{\partial t} + \frac{\partial(\bar{\rho}\tilde{U}_i\tilde{k})}{\partial x_j} &= \frac{\partial}{\partial x_j} \left( \frac{\mu_t}{\sigma_k} \frac{\partial\tilde{k}}{\partial x_j} \right) \\
+ \mu_t \left( \frac{\partial\tilde{U}_i}{\partial x_j} + \frac{\partial\tilde{U}_j}{\partial x_i} \right) \frac{\partial(\tilde{U}_i)}{\partial x_j} - \frac{2}{3} \left( \mu_t \frac{\partial\tilde{U}_k}{\partial x_k} \right) \frac{\partial\tilde{U}_m}{\partial x_m} &+ C_{BVG} \mu_t \frac{\|\bar{\nabla}\rho \times \bar{\nabla}p\|}{\rho^2} - \frac{2}{3} \bar{\rho}\tilde{k} \frac{\partial\tilde{U}_m}{\partial x_m} - \bar{\rho}\tilde{\varepsilon}
\end{aligned}$$

Eq. 10

$$\begin{aligned}
\frac{\partial(\bar{\rho}\tilde{\varepsilon})}{\partial t} + \frac{\partial(\bar{\rho}\tilde{U}_i\tilde{\varepsilon})}{\partial x_j} &= \frac{\partial}{\partial x_j} \left( \frac{\mu_t}{\sigma_\varepsilon} \frac{\partial\tilde{\varepsilon}}{\partial x_j} \right) \\
+ C_{\varepsilon 1} \frac{\tilde{\varepsilon}}{\tilde{k}} \left[ \mu_t \left( \frac{\partial\tilde{U}_i}{\partial x_j} + \frac{\partial\tilde{U}_j}{\partial x_i} \right) \frac{\partial(\tilde{U}_i)}{\partial x_j} - \frac{2}{3} \left( \bar{\rho}\tilde{k} + \mu_t \frac{\partial\tilde{U}_k}{\partial x_k} \right) \frac{\partial\tilde{U}_m}{\partial x_m} \right] &+ C_{\varepsilon 3} \mu_t \frac{\tilde{\varepsilon}}{\tilde{k}} \frac{\|\bar{\nabla}\rho \times \bar{\nabla}p\|}{\rho^2} - \bar{\rho} C_{\varepsilon 2} \frac{\tilde{\varepsilon}}{\tilde{k}} \tilde{\varepsilon}
\end{aligned}$$

Eq. 11

These equations are standard except for the terms in Eq. 10 and 11 with density gradients crossed with pressure gradients. For the validation portion of this study, these terms were set to zero, resulting in the standard model. However, they are retained here because their effect is studied and presented in the discussion section of this report.

The goal for this study is to narrow the filter width such that only part of the turbulent spectrum is modeled, and the balance resolved. As the RANS limit is approached, due to the ergodicity assumption, all terms vanish in Eq. 7 except the Reynolds stresses, and in the DNS limit, all the stresses must become vanishingly small. To produce a simple model with the correct limiting behavior in the RANS limit, an argument will be made that near the RANS limit, the non-linear terms requiring modeling are a perturbation from the ergodic limit.

Since the Leonard and cross-stresses vanish in the ergodic RANS limit, it will be assumed that these terms are second order relative to the Reynolds stresses and can be ignored for applications where the filter width is not too far from the integral turbulence time scale, i.e., integral scale eddy rollover time. The intended application space of these models is to resolve the lowest frequency modes for which the filter width will be a tenth to a hundredth of the integral scale eddy rollover time. With relatively few dynamical modes present, the authors assume that the Leonard and cross-stresses will be small and will treat them as zero. It is acknowledged that we have not demonstrated that the Leonard and cross stresses are small relative to the Reynolds stresses over the intended operational space. However, the perturbation argument holds in the near RANS limit, the deviation becomes increasingly unimportant in the near DNS limit (as the modeled stresses vanish). Note that the assumption that the Leonard and cross-stresses can be ignored is commonly employed by the LES community in between these limits with less formal justification than is discussed here.

The substitution of the filtered quantity by a model, as shown in Eq. 12, must be done carefully with consideration to the physics of the modeled quantities. In Eq. 12, all terms are composed of filtered quantities, where the filter width,  $\tau$ , must be taken into consideration.

$$\begin{aligned}
 -\rho \widetilde{u_i'' u_j''} &\equiv -\frac{1}{\bar{\rho}} \int_{-\infty}^t \rho(\tau) G(t, \tau) u_i''(\tau) u_j''(\tau) d\tau \\
 &\equiv \widetilde{k} \left[ C_{\mu} \bar{\rho} \frac{\widetilde{k}}{\widetilde{\varepsilon}} \left( \frac{\partial \widetilde{U}_i}{\partial x_j} + \frac{\partial \widetilde{U}_j}{\partial x_i} - \frac{2}{3} \frac{\partial \widetilde{U}_k}{\partial x_k} \delta_{ij} \right) - \frac{2}{3} \bar{\rho} \delta_{ij} \right]
 \end{aligned}
 \tag{Eq. 12}$$

The decomposition suggested by Eq. 12 into the product of the subfilter (modeled) turbulent kinetic energy and the term in square brackets is deliberate. In the RANS limit, Eq. 12 will be identical to Eq. 8 only if the modeled turbulent kinetic energy and the mean velocity gradients match the RANS definitions. In the DNS limit, the product of the terms must go to zero to recover the Navier-Stokes equations. However, in the DNS limit in a turbulent flow, neither the velocity gradients nor the turbulent kinetic energy are zero. From these facts, it is clear that,  $\widetilde{k}$ , must represent only the *subfiltered or modeled* portion of the turbulent kinetic energy spectrum. In the RANS limit, the full spectrum of the turbulent kinetic energy is modeled, and  $\widetilde{k}$ , and its source and sink terms have their usual definition in Eq. 10. In the DNS limit, the full spectrum of the turbulent kinetic energy is resolved as the velocity gradients approach their Navier-Stokes counterparts. In this case, the turbulent kinetic energy spectrum also becomes resolved and the modeled turbulent kinetic energy,  $\widetilde{k}$ , is zero. For this limit to occur,  $\widetilde{k}$  and its source and sink terms in Eq. 10 need to be a function of the filter width,  $\tau$ .

Eq. 10 gives the dynamical behavior of the turbulent kinetic energy. Its advection and diffusion are controlled by velocity gradients. These gradients will limit to their correct behavior, if the velocities limit to their correct behavior, which in turn depends on the turbulent kinetic energy limiting to its correct behavior. Thus, the key to producing the correct limits resides in producing source and sink terms for the turbulent kinetic energy that have the correct limiting behavior. If the source and sink terms correctly approach their limits, the system of equations will approach the desired limits. In Eq. 10, the production term (all right hand side of Eq. 10 except the first and last terms) is a model, and the sink term,  $-\rho \varepsilon$ , is given by Eq. 11. Eq. 11 is in itself a modeled equation. The actual dissipation equation can be derived but cannot be suitably closed.

Figure 3 shows a notional physical interpretation of the behavior of the production term in Eq. 10. The actual production of turbulent kinetic energy occurs over a spectrum of time (or equivalently, length) scales. At the high end of the frequency spectrum, production of turbulent kinetic energy vanishes as the dissipation scales are reached. At the lowest end of the spectrum, there is also a limit to the production that is perhaps less obvious. A simple example is illustrative. Most simple flows such as jets and plumes reach a self-similar regime. For example, for a given size of jet, the turbulence is bounded by the jet diameter. Production of turbulence in such a jet does not occur at larger scales

than the jet diameter. Similarly, in a temporal sense, there is a lowest frequency mode corresponding to these largest eddies. There is no production in lower frequencies corresponding to larger time scales. The authors interpret this low frequency production cutoff in terms of the eddy rollover time, which is given by  $\tilde{k} / \tilde{\varepsilon}$ .

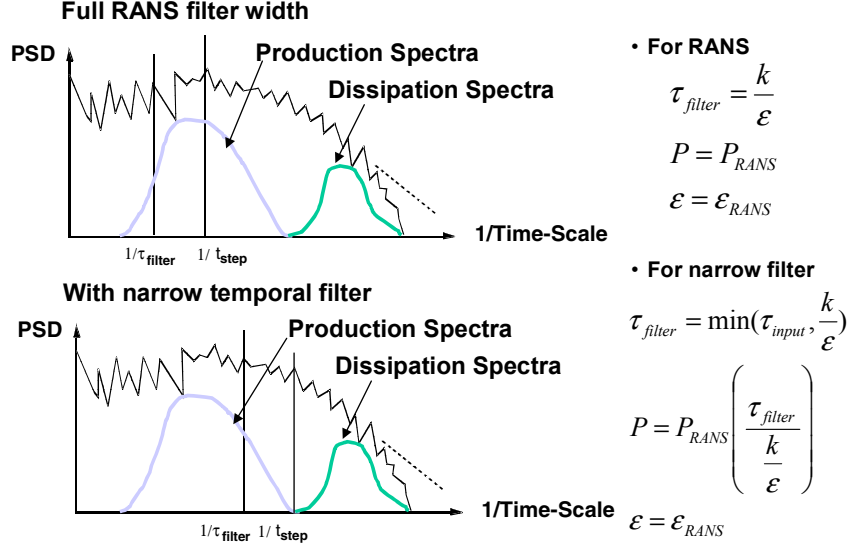


Figure 3. Interpretation of the Production Term in the Turbulent Kinetic Energy Equation for TFNS

Equation 13 recasts the production term in Eq. 10 in terms of the eddy rollover time,  $\tilde{k} / \tilde{\varepsilon}$ .

$$P = C_\mu \bar{\rho} \tilde{k} \left( \frac{\tilde{k}}{\tilde{\varepsilon}} \right) \left[ \left( \frac{\partial \tilde{U}_i}{\partial x_j} + \frac{\partial \tilde{U}_j}{\partial x_i} \right) \frac{\partial (\tilde{U}_i)}{\partial x_j} - \frac{2}{3} \left( \frac{\partial \tilde{U}_k}{\partial x_k} \right) \frac{\partial \tilde{U}_m}{\partial x_m} + C_{BVG} \frac{\|\vec{\nabla} \rho \times \vec{\nabla} p\|}{\rho^2} \right] - \frac{2}{3} \bar{\rho} \tilde{k} \frac{\partial \tilde{U}_m}{\partial x_m} \quad \text{Eq. 13}$$

Production of turbulent kinetic energy is often described (cf., Tennekes and Lumley, 1972) in terms of vorticity stretching induced by mean flow gradients. A physical interpretation of Eq. 13 is given in Eq. 14.

$$P \sim \left[ \tilde{k} \left( \frac{\partial \tilde{U}_i}{\partial x_j} + \frac{\partial \tilde{U}_j}{\partial x_i} \right) \right] \left[ \frac{\partial (\tilde{U}_i)}{\partial x_j} \left( \frac{\tilde{k}}{\tilde{\varepsilon}} \right) \right] \sim \left[ \frac{\tilde{k}}{t_{prod}} \right] \left[ \frac{1}{\bar{\rho}} \int_{-\infty}^t \rho(\tau) G(t, \tau) f_{prod}(\tau) d\tau \right] \sim \left[ \frac{\tilde{k}}{t_{prod}} \right] [f_{prod} \tau] \quad \text{Eq. 14}$$

The production term can be thought of as a product of the amplitude for a given stretching event and the total number of such events. The amplitude of the production term for a given stretching event is denoted by the first bracketed term in each of the proportionalities in Eq. 14. The amplitude (i.e., the rate of change of turbulent kinetic

energy given an event) is derived from a stretching (represented by velocity gradients) of the vorticity (represented by the turbulent kinetic energy). The total number of such stretching events is given by the second term. It is simply the frequency of events,  $f_{prod}$ , *integrated over the timescale of interest, which in this case is the filter width,  $\tau$* .

In the limit where the filter width is as wide as the eddy rollover time,  $\tilde{k} / \tilde{\epsilon}$ , Figure 3 shows that the full production spectrum is modeled, and the RANS limit is recovered. For narrower filter widths, only part of the production spectrum is modeled and the balance is resolved. In the limit of vanishing filter widths, the modeled portion of production vanishes, shutting down the source term for the modeled turbulent kinetic energy.

Associating the filter width with the definition of turbulent viscosity, the result is

$$\mu_t = C_\mu \bar{\rho} \tilde{k} \text{Min} \left( \tau, \frac{\tilde{k}}{\tilde{\epsilon}} \right) \quad \text{Eq. 15}$$

where the minimum function ensures that for filter widths longer than the RANS limit, the physical limits of turbulence saturation are recovered.

In addition to the production term, the eddy viscosity also appears in the closure term for the Reynold stresses. Mathematical consistency requires that Eq. 15 define the eddy viscosity here as well. However, beyond mathematical consistency, there is a clear physical interpretation of using Eq. 15 in this context. The traditional physical argument for the eddy viscosity is that it is a product of a fluctuating velocity times an eddy length scale. In the context of Eq. 15, the fluctuating velocity is defined by the square root of the turbulent kinetic energy and the length scale is by the square root of the turbulent kinetic energy allowed to propagate for the time corresponding to the temporal filter.

Strictly speaking, as the DNS limit is approached, vanishing production assured by Eq. 15, is not sufficient to ensure the correct limiting behavior. The dissipation must also be addressed. As the limit is approached, Prof. Bill Jones (private communication) notes that Eq. 15 could be modified such that the temporal filter width is modified by the ratio of  $C_{\epsilon 2} / C_{\epsilon 1}$ , thus ensuring that the ratio of production to dissipation is in balance in this limit. Also note that it is somewhat inefficient to use a complex set of transport equations to capture the velocity fluctuations near the DNS limit, since only dissipation is occurring. A reconstruction method such as that by Pruett and colleagues (Pruett, et al., 2003) will be more effective in the near DNS limit. In the current study, we are in the near RANS limit and use Eq. 15 in its simplest form.

Simulations by a number of authors using Eq. 9 instead of Eq. 15 have shown dynamic behavior. The simulations are often referred to as Unsteady RANS, or URANS calculations. The rationale given is that as the mesh density is increased and the time step decreased, Eqs. 8 – 11 will naturally migrate to the correct balance between modeled and resolved physics and become increasingly dynamic. The use of Eq. 15 in place of Eq. 9 overcomes a number of weaknesses with this argument. Since it is based on an ergodicity assumption, the RANS limit should be steady, independent of mesh density. The fact that

the numerical simulation is not steady may have more to do with the coefficients used in the standard models, than any physics. Eq 15 ensures that the split between modeled and resolved production spectra are cleanly separated and there is no double consideration that may occur when using Eq. 9, which assumes that the full spectrum is modeled, while some production is resolved on the grid.

The form of Eq. 15 will not be a surprise to the LES community, as it is a temporal analog to a commonly used LES SGS closure model (cf., Deardorff, 1980). In the limiting case of homogeneous, isotropic turbulence with no mean flow, the relationship between a spatial filter and temporal filter is given by fluctuating velocity. Using the square root of the turbulent kinetic energy,  $k$ , as a measure of this velocity, the temporal filter becomes an equivalent spatial filter with a width corresponding to

$$l = \tau \sqrt{\tilde{k}} \quad \text{Eq. 16}$$

Substituting Eq. 16 into Eq. 15, for values of the time filter smaller than characteristic eddy turn over time results in

$$\mu_t = C_\mu \bar{\rho} \sqrt{\tilde{k}} l \quad \text{Eq. 17}$$

Using Eq. 15 in place of Eq. 9 constitutes the set of equations to be used for the TFNS simulations in this study. In keeping with the desire to have a constant filter width in order to separate numerical from modeling error, the filter width is entered as a user parameter, and the time step is fixed to less than half the value of the filter width.

## ***Numerical Implementation***

SIERRA/Fuego is a low-Mach number, turbulent reacting flow code using the Favre-averaged form of the unsteady transport equations describing the transport of heat, mass, and momentum. The governing turbulent transport equations are written in integral form and discretized on unstructured meshes using a control volume finite element method (CVFEM) cf., Moen, et al., 2002.

An illustrative 2D control volume with associated elements is shown in Fig. 4. Primitive variables are located at the vertices of the finite elements. The finite volumes are centered about the nodes and are assembled on an element-by-element basis. The integration points are determined by the surfaces connected between the element centroid, the element face centroids, and the edge centroids. Therefore, integration points, over which surface fluxes are evaluated, are located at sub-face centers. Linear shape functions are used for the interpolation of properties and the computation of gradients within the element.

A segregated, approximate projection scheme is the numerical solution method. Since the primitive variables are collocated, a modified momentum interpolation method (Moen, et al., 2002) is employed to avoid pressure-velocity decoupling. The effect of this method is to add a pressure stabilizing term that is proportional to the fourth order spatial derivative of pressure.

For the current study, a backward Euler time integration approach is used that includes the effect of variable density. This method is first order accurate in time and is commonly employed to obtain RANS solutions. Time accurate solutions are obtained through Picard looping. In the present study, no less than 5, and in most cases 8, Picard loops were taken for each time step. With Picard looping, the method remains formally first order, but the error will be reduced in proportional to the number of Picard loops taken.

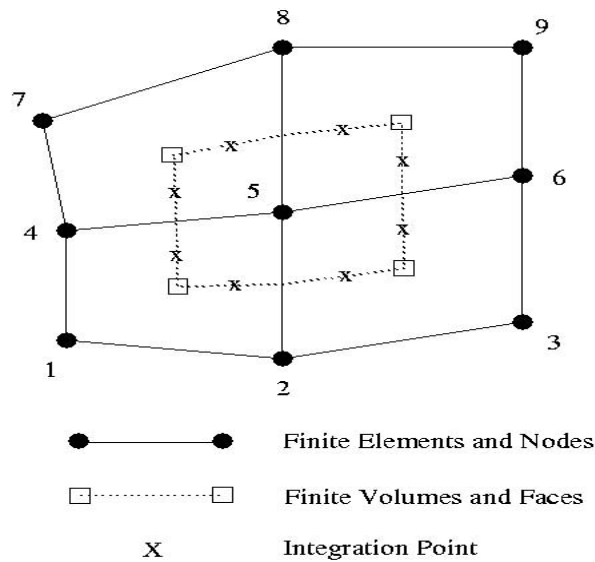


**Figure 4. Sample 2D control volume definition used in the CVFEM element-based technique**

Several upwind schemes are supported for the evaluation of convective fluxes at integration points. Each upwind method is blended with a centered scheme as the cell Peclet number falls below two. In general, assembling element-by-element, in lieu of neighbor contributions, limits the order of the convection coefficient. The supported standard methods include first order upwind and a skew upwind approach that requires element face intersections.

For all simulations in this study a MUSCL upwind approach (cf. Hirsh, 1990), which requires pre-assembly of gradient information at nodes, was used. The MUSCL scheme was limited with a Van Leer type limiter and blended 80% MUSCL and 20% first order upwind. Even though the MUSCL scheme is second order, its upwind nature is quite dissipative relative to energy preserving schemes such as a fully central difference

operator. LES simulations will employ an energy preserving scheme to minimize the numerical dissipation. For the current study, it was decided to employ typical RANS type numerics. Future efforts will look at the effect of employing more energy preserving schemes.

A verification test suite was completed prior to this validation study. The implementation of the temporal filter through the eddy viscosity definition (Eq. 13) was verified by post-processing the results to ensure that the filter time was constant. In addition, some twenty verification problems considered relevant to the current helium plume study were completed prior to this study. These problems include:

### **Steady Flow Problems**

#### **1.0 Laminar Diffusion, Mass Transport, Variable Properties**

**Diffusion of Species to a Wall:** Tests multiple species mixing  
One-dimensional; Analytical Solution

#### **2.0 Laminar Convection-Diffusion, Thermal Transport, Constant Properties**

- a) **Buoyant Plume:** Tests diffusion-convection/thermal coupling and open B. C.'s  
Two-dimensional; Analytical solution away from the point source
- b) **Flow in a Cube:** Tests order of accuracy of diffusion-convection operators  
Three-dimensional; Manufactured Solution

#### **3.0 Laminar Convection-Diffusion, Mass Transport, Variable Properties**

**Species Plume:** Tests diffusion-convection/species coupling and open B. C.'s  
Two-dimensional; Analytical solution away from the point source

#### **4.0 Turbulent Convection-Diffusion, Isothermal, Constant Properties**

- a) **Turbulent Round Jet:** Tests fluid flow/ $k$ - $\epsilon$  model coupling  
Three-Dimensional; Numerical Benchmark Solution (CFX); Includes Wall Fxn.
- b) **BVG Model:** Test implementation of an algebraic turbulence model  
Unit test comparisons against hand calculations

## Validation

The goal of this validation study is to quantify the uncertainty in using the developed temporally filtered closure model in a flow relevant to fires. As noted in Tieszen, et al., 2001, fires can be classed as reacting plumes. By validating the turbulence model in a non-reacting plume, the effect of buoyancy-generated turbulence can be tested independent of the complexity introduced by turbulent combustion. This validation study is the first in a series of validation problems of increasing physical complexity.

### **Experimental Data Summary**

The experimental data set used for comparison was developed at Sandia National Laboratories by the Weapons Engineering Certification Campaign explicitly for use in validating the turbulence models for SIERRA/Fuego/Syrinx. The experiments and results are discussed in O'Hern, et al., 2004, and briefly summarized here as relevant.

The experiments were performed in the Fire Laboratory for Model Accreditation and Experiments (FLAME), which is shown in Fig. 5. A schematic of the experiments is shown in Fig. 6. Multiple repeat tests were conducted (4 full data sets) at a single test condition for which the average Richardson number is  $Ri = (\rho_\infty - \rho_p)gD/(\rho_\infty V_0^2) = 70$ , where  $\rho_\infty$  is the external (air) density,  $\rho_p$  is the plume (helium) density,  $D$  is the diameter of the plume source (1 meter),  $V_0$  is the inlet velocity, and  $g$  is gravitational acceleration. Planar Laser Induced Fluorescence (PLIF) diagnostics required adding tracers to the helium plume. Acetone is used as the fluorescent tracer gas, seeded into the main helium flow at  $1.7 \pm 0.1$  volume percent. In addition,  $1.9 \pm 0.2$  volume percent oxygen is added to quench acetone phosphorescence. The molecular weight of the plume gases (helium/acetone/oxygen mixture) is  $5.45 \text{ g/mol} \pm 2.7\%$ . The average mixture Reynolds number at the plume source is  $Re = DV_0/\nu = 3200$ , where  $D$  is the diameter of the plume source (1 meter),  $V_0$  is the inlet velocity, and  $\nu$  is the kinematic viscosity of the helium/acetone/oxygen mixture. The average inlet velocity is  $0.34 \text{ m/s} \pm 2.4\%$ .

Two-dimensional velocity fields were measured using particle image velocimetry (PIV). Helium mass fraction was determined by seeding the helium with acetone vapor and measuring planar laser-induced fluorescence (PLIF) from the acetone. PIV and PLIF were performed simultaneously using a 200 Hz XeCl excimer laser and 35-mm motion picture cameras. The film images were digitized and post-processed to obtain velocity and mass fraction data on a vertical plane approximately 0.8 m high by 1 m wide centered laterally on the plume centerline and extending upward from the plume source to include the pure helium core, near-field mixing zones, and surrounding air as shown in Fig. 6.

The resulting data to be used for model comparisons are shown in Fig. 7 – 10. The data consists of the Favre-averaged vertical and horizontal velocities, the time-averaged density field, and an estimate of the Favre-averaged turbulent kinetic energy. The latter has been estimated by assuming that the out-of-plane horizontal fluctuations are the same as the measured inplane horizontal fluctuations. This estimation is expected to be valid,

primarily because the vertical fluctuations are approximately an order of magnitude larger than the horizontal fluctuations, so the results will be insensitive to this assumption.



**Figure 5. Photograph of the Fire Laboratory for Accreditation of Models and Experiments (FLAME).**

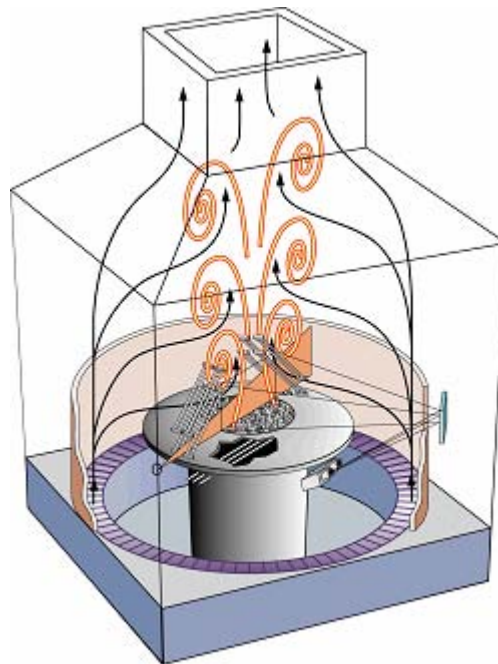


**Figure 6. Schematic of the Flame Facility Showing Relationship of Plume, Laser Illumination, and Cameras.**

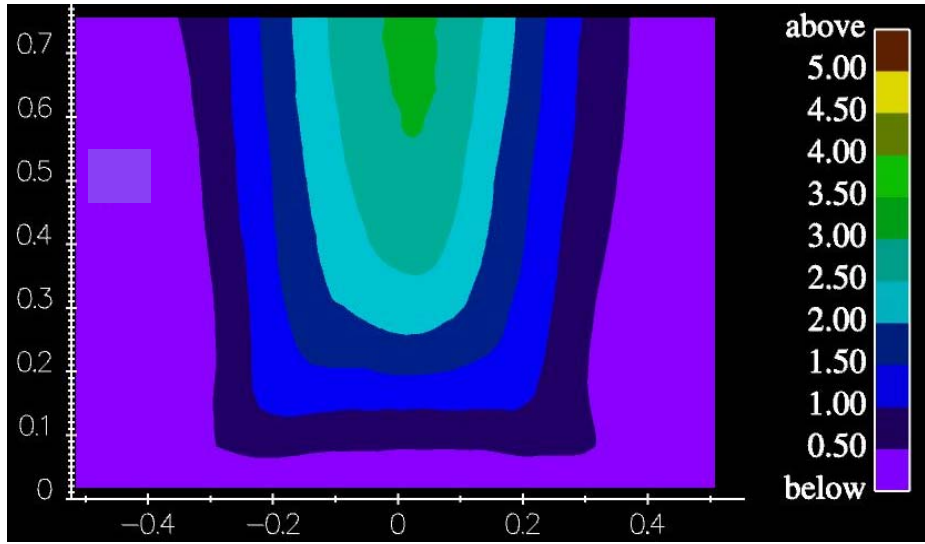


Figure 7. Favre-averaged Vertical Velocity Profile Data (m/s)

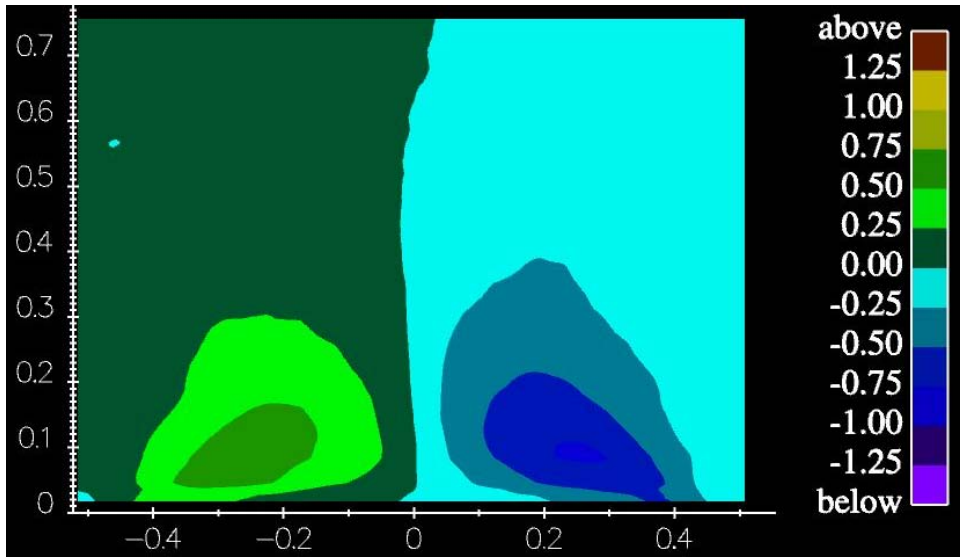


Figure 8. Favre-averaged Horizontal Velocity Profile Data (m/s)

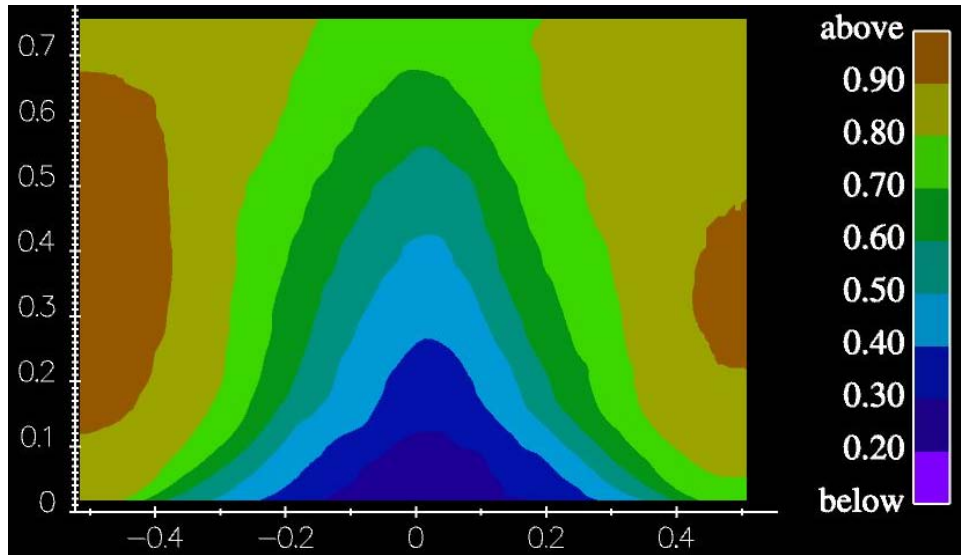


Figure 9. Time-averaged Plume Density Profile Data ( $\text{kg/m}^3$ )

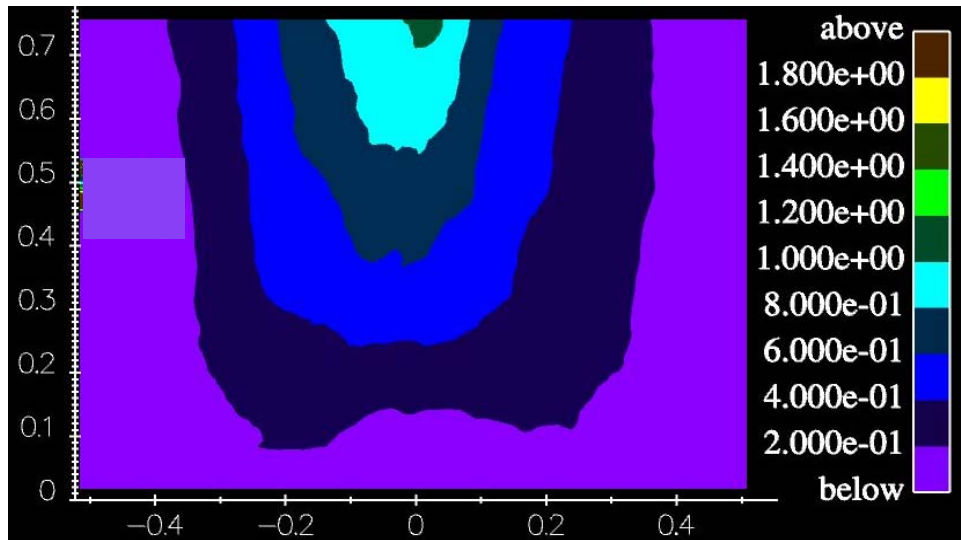


Figure 10. Favre-averaged Turbulent Kinetic Energy Profile Estimate ( $\text{m}^2/\text{s}^2$ ). The estimate assumes that the out of plane horizontal fluctuations are equal to the inplane estimates.

The uncertainty in the experimental velocities is  $\pm 20\%$ . The uncertainty in the values of plume density is  $\pm 18\%$  of the measured concentration plus a fixed uncertainty of  $\pm 5\%$ .

The uncertainty in the turbulent kinetic energy estimate is  $\pm 30\%$ . These uncertainties are larger than typical for PIV and PLIF; however, it must be kept in mind that this is a unique large-scale application of these diagnostics. The uncertainties also contain test-to-test variabilities.

### Validation Simulation Matrix

The validation simulation matrix is shown in Fig. 11. Since the data acquired exists for one realization of the boundary conditions, there is nominally only one set of experimental parameters for which the model and data are to be compared.

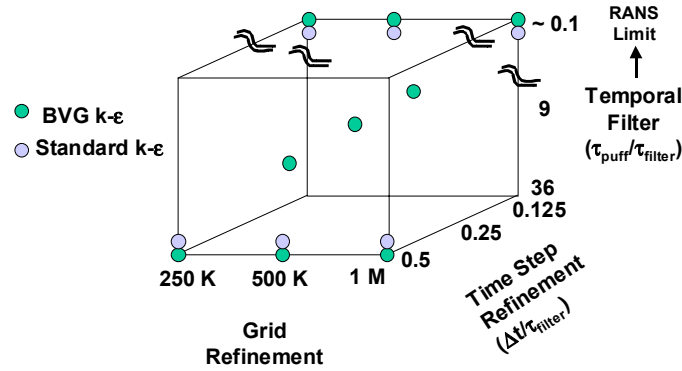
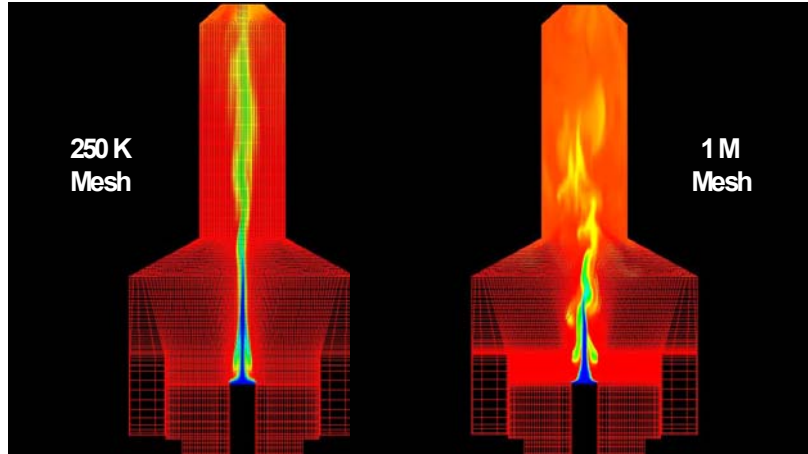


Figure 11. Validation Simulation Matrix

As shown in Figure 11, there are two model formulations and two numerical parameters in the test matrix. The turbulence model is used with and without a term for buoyant vorticity generation (i.e., Eq. 10 & 11, with  $C_{BVG}$  and  $C_{\epsilon 3}$  set to zero, or  $C_{BVG}$  and  $C_{\epsilon 3}$  set to 0.35 and zero, respectively), and the temporal filter width,  $\tau_{filter}$ , that results as a model parameter in TFNS (Eq. 15). The numerical parameters include grid and time step refinements. In this section, comparisons will be made with the standard k- $\epsilon$  model only, while comparisons to the BVG modified model will be made later in the discussion section.

In this study, the model filter will be varied at two levels,  $\tau_{filter} = 0.02$  and  $0.08$  seconds. To provide context, the time required to complete a puff cycle,  $\tau_{puff}$ , for this plume is  $0.73$  seconds (O’ Hern, et al., 2004). The ratio of the temporal filter width to the puffing period ( $\tau_{puff} / \tau_{filter}$ ) is nominally  $36$  and  $9$  respectively. The puffing period represents the slowest turbulence mode in the flow and the filter width chosen permits  $36$  and  $9$  filter widths per puff, respectively. The results of this study can be compared to that of Nicolette, et al., 2004. In that study, the authors attempted to simulate the plume in a steady state manner. The upper row of simulations indicated in Figure 11 is from that study and will be discussed later. Nominally, this flow can be considered steady state if a statistically significant number of the slowest model structures have passed (i.e., puff cycles have occurred.) Hence, the nominal value of  $\sim 0.1$  is shown on the top row of the simulations in Figure 11.

To understand the sensitivity to the grid, three grid levels were proposed, nominally, 250 K, 500K, and 1 M, node meshes. In addition, a single run was performed for a 2 M node mesh. The strategy employed in refining the grid is to locally double the mesh in all three coordinate directions within the 1 m diameter plume for the first meter above the helium source. The mesh was then stretched from this refined grid to the same coarse outline of the facility. Hence the near field of the plume is highly refined, while the facility itself is only coarsely meshed. The result is shown in Figure 12.



**Figure 12. Comparative Mesh Densities (with gas density contours overlaid).**

While unstructured grids can be used in Fuego, the meshes used in this study were built using a structured grid generator (with body fitted coordinates). By using a structured grid generator, an all hexahedral mesh was produced. It was necessary to use an all hexahedral mesh at the time this study was conducted because the tetrahedral element formulation had not been verified. The unfortunate consequence of structured grids is that high element densities were produced in regions away from the region of interest, such as the chimney.

The grid refinement study was performed with a constant time step,  $\Delta t$ , of 0.01 second with a filter width,  $\tau_{filter}$ , of 0.02 seconds, for a ratio of  $(\Delta t / \tau_{filter})$  of 0.5, as shown in Figure 11. Since these are transient simulations, it is also necessary to show time step refinement. To be computationally affordable, the time step refinement study was conducted using the medium (500K node) mesh with the temporal filter width,  $\tau_{filter}$ , of 0.08 seconds. Time steps of 0.04, 0.02 and 0.01 seconds were used resulting in a ratio of  $(\Delta t / \tau_{filter})$  of 0.5, 0.25, and 0.125 respectively.

## Simulation Results and Data Comparisons

### Mesh Refinement Study

Simulation results for the grid refinement study using the standard k- $\epsilon$  model are shown in Figures 13 – 17. Figure 13 shows the Favre-averaged vertical velocity profiles for the 250K, 500K, 1M, and 2M node mesh results. To obtain the result in Figure 13, instantaneous spatially resolved data, as shown in Figure 14, were density weighted and time-averaged. The durations of the time averages vary but are similar to the duration over which the data were obtained. As can be seen in Figure 13, the results are non-monotonic with increasing mesh density. The non-monotonicity in the Favre-averaged results occurs because different dynamic modes are selected by the flow at different mesh densities.

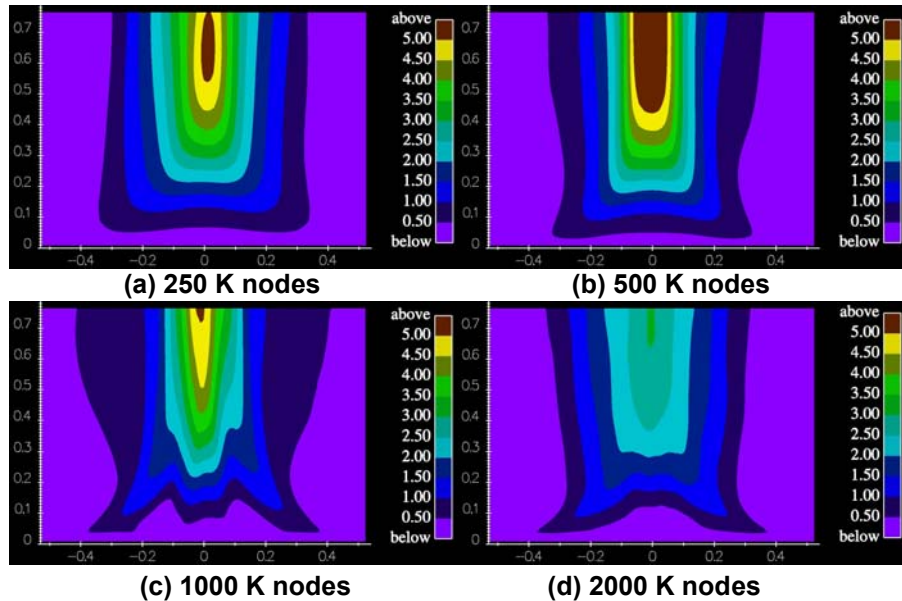


**Figure 13. Favre-averaged Vertical Velocity (m/s) Profiles.**  
(a) 250K (b) 500K (c) 1M and (d) 2M node meshes. Temporal Filter = 0.02 sec,  $\Delta t = 0.01$  sec.

Dynamics are difficult to show in two-dimensional images. Figure 14 shows instantaneous density fields with overlaid velocity vectors illustrating the dynamics that can be clearly seen in the simulations. For the 250K mesh in Figure 14(a), the results show an asymmetric mode. The consequence of this asymmetry is that the plume centerline is deflected from the vertical resulting in ambient fluid crossing the centerline, reducing the peak velocity and plume concentration relative to a symmetric mode.

For the 500K mesh in Figure 14(b), the mode is symmetric. Figure 14(c) is also symmetric, but shows larger scale structures. Figure 14(d) is primarily symmetric but with chaotic smaller scale features that produce asymmetries. The images are at approximately the same phase in the puffing cycle.

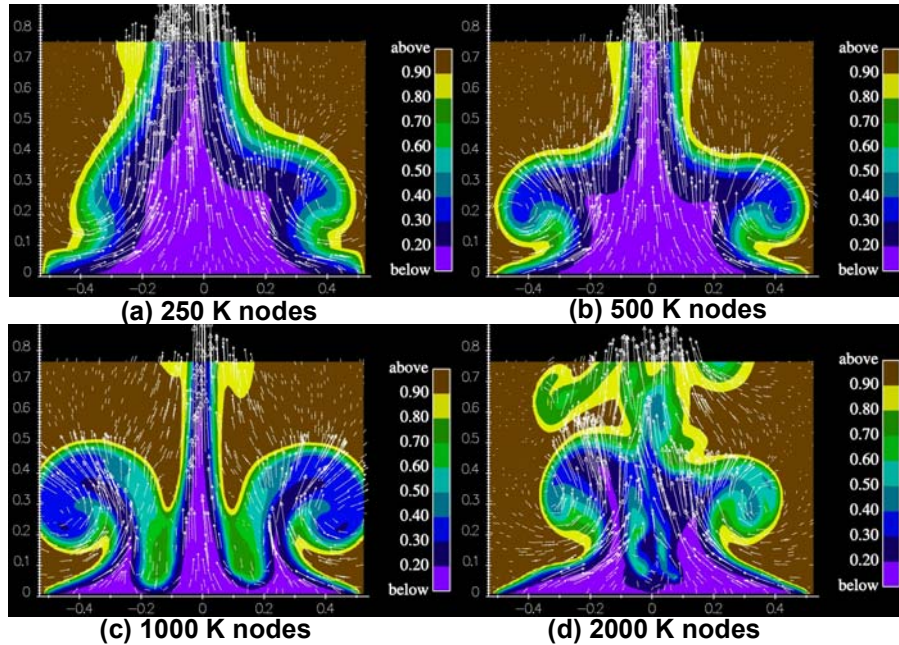


**Figure 14. Instantaneous Density Profiles ( $\text{kg/m}^3$ ) and Vertical Velocity Vectors.**  
 (a) 250K (b) 500K (c) 1M and (d) 2M node meshes. Temporal Filter = 0.02 sec,  $\Delta t = 0.01$  sec.

Figure 15 shows the horizontal velocity component for the mesh refinement study. Clearly the largest entrainment is at the base of the plume. As the mesh density is increased from 250K to 1M, the horizontal velocity peak becomes more pronounced.

Figure 16 shows the gas density profiles for the mesh refinement study. Comparing Figure 16 with Figure 13, it can be seen that the density and vertical velocity are well correlated. For the 250K mesh, in which the asymmetric mode decreases the peak centerline vertical velocity, the plume concentration along the centerline is also reduced compared to the 500K mesh that is characterized by the symmetric puffing mode. As the mesh is increased to 1M and to 2M nodes, smaller scale asymmetries result in a decrease in the plume concentration along the centerline.

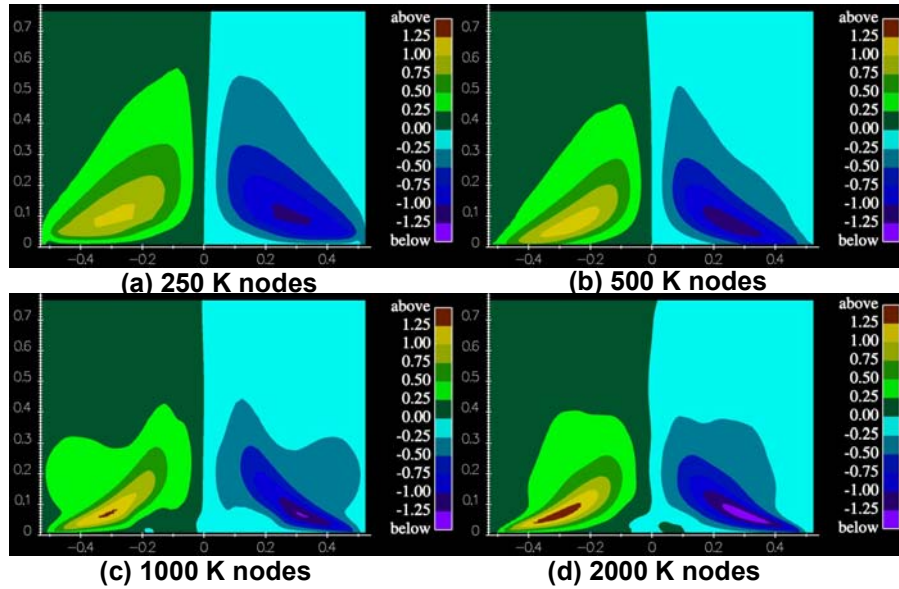


Figure 15. Favre-averaged Horizontal Velocity (m/s) Profiles.  
 (a) 250K (b) 500K (c) 1M and (d) 2M node meshes. Temporal Filter = 0.02 sec,  $\Delta t = 0.01$  sec.

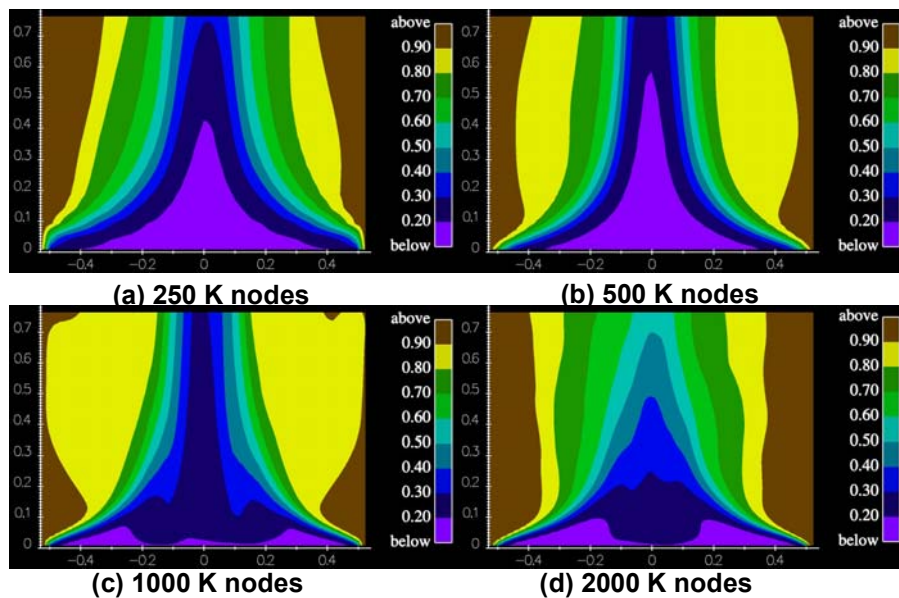
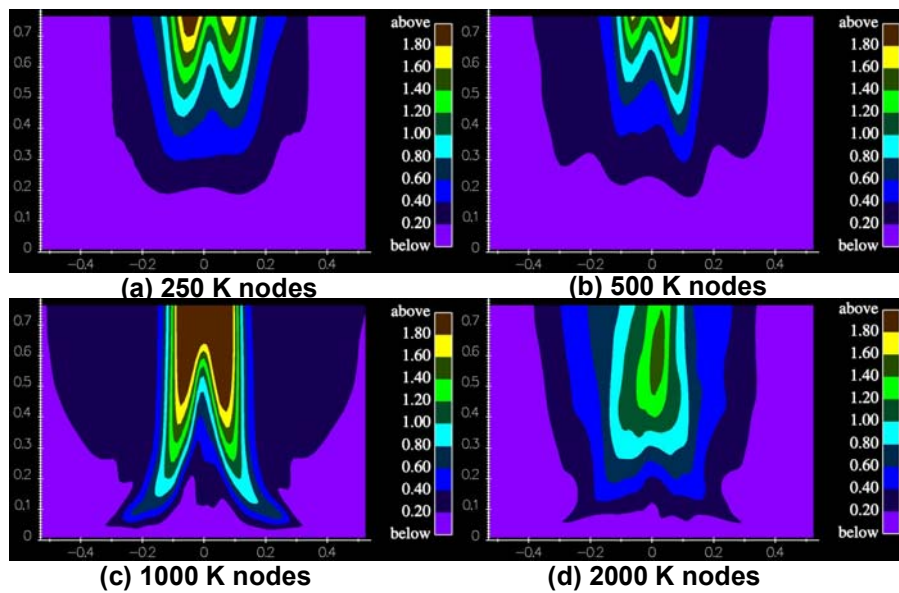


Figure 16. Time-averaged Density ( $\text{kg/m}^3$ ) Profiles.  
 (a) 250K (b) 500K (c) 1M and (d) 2M node meshes. Temporal Filter = 0.02 sec,  $\Delta t = 0.01$  sec.

Figure 17 shows the turbulent kinetic energy profiles for the mesh refinement study. To be consistent with the data, the turbulent kinetic energy is calculated from the two in-

plane velocity variance components and setting the horizontal out of plane velocity variance component equal to the horizontal in-plane velocity variance component and summing and dividing by two to get the turbulent kinetic energy. The turbulent kinetic energy profiles are calculated from the Favre fluctuations and represent Favre-averages. As a second order statistic, i.e. the variance of the velocity fluctuations, it can be expected to be less converged than the mean velocity statistics. Relative to mesh refinement, this lack of convergence is evident, as the spatial distributions for each mesh level appear to be quite different. The more diffuse profile of the highest mesh density, 2M nodes, is a result of the presence of more dynamics within the simulation compared to coarser meshes.



**Figure 17. Favre-averaged Turbulent Kinetic Energy ( $\text{m}^2/\text{s}^2$ ) Profiles.**  
 (a) 250K (b) 500K (c) 1M and (d) 2M node meshes. Temporal Filter = 0.02 sec,  $\Delta t = 0.01$  sec.

For convenience, side-by-side comparisons between the data (on the left) and two million node simulation (on the right) are shown in Figure 18. This figure is useful for qualitative comparison purposes. Overall, the predicted vertical velocity profiles are close to the data. The predicted horizontal velocity profiles are narrower and of higher amplitude than the data. The predicted density profile shows a slower centerline decay of plume fluid (i.e., increase in density) than the data. Given that it's a second order statistic, the predicted turbulent kinetic energy profile is similar to the data.

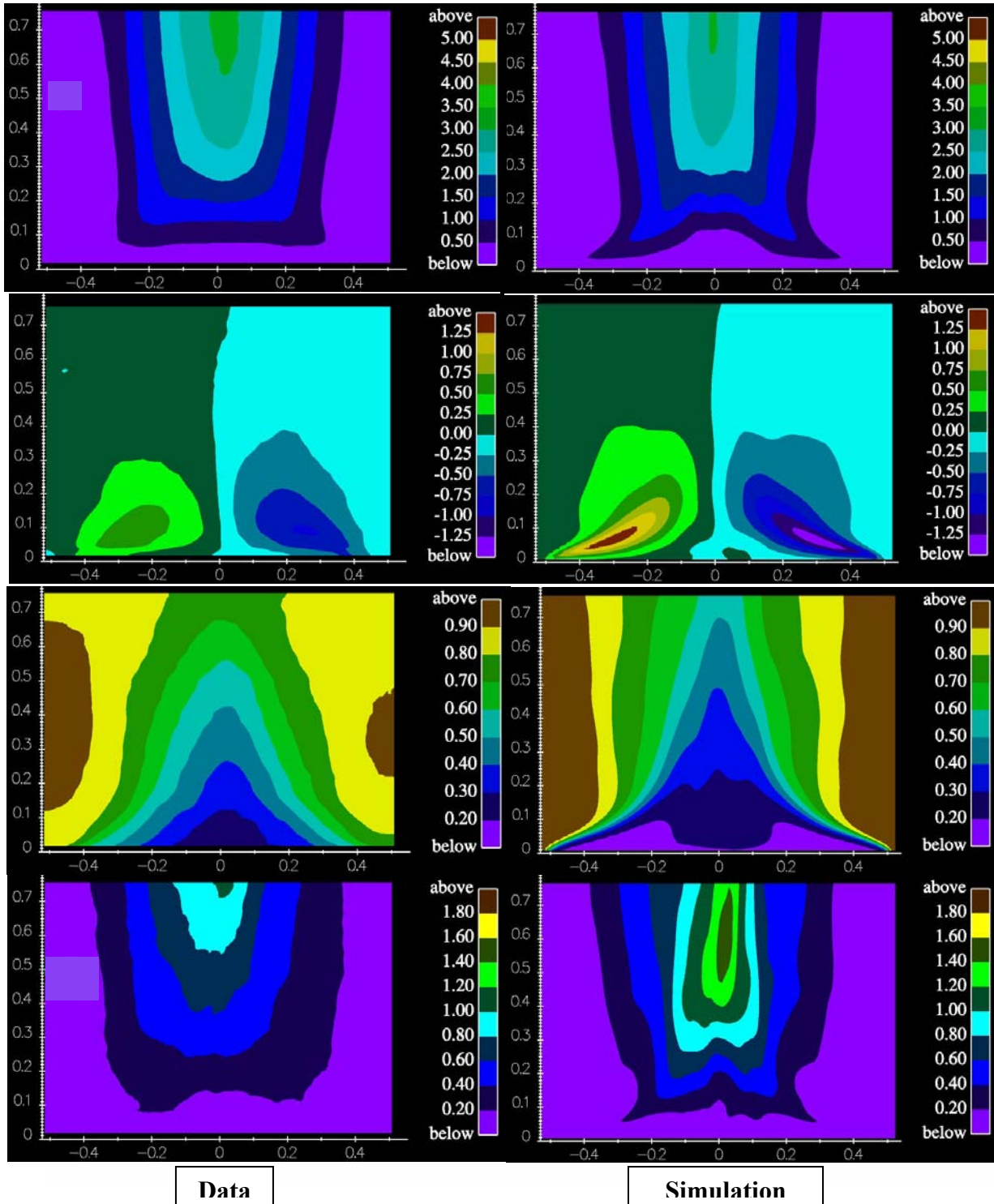
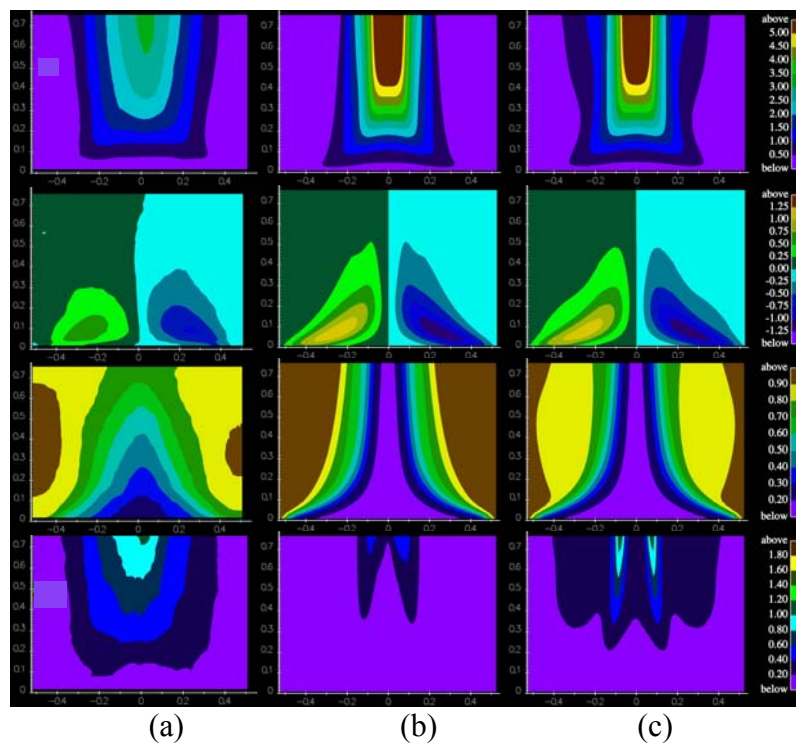


Figure 18. Comparison of Data and 2M Node Simulation Results. Top to Bottom: Vertical Velocity (m/s), Horizontal Velocity (m/s), Density ( $\text{kg/m}^3$ ), and Turbulent Kinetic Energy ( $\text{m}^2/\text{s}^2$ ). Data on left, 2M node simulation results on right.

The discrepancies can be attributed to missing small scale vortical structures at the edge of the plume near the base. These vortical structures are clearly visible in the movies of the data and are missing from the simulations. Underpredicting this mixing results in narrow high velocity radial indraw, sharp density profiles near the base, and a delay in the decay of the centerline plume concentration (i.e., increase in centerline density).

### Time Step Refinement Study

The time step refinement study was conducted with the 500K node mesh density for a fixed temporal filter width of 0.08 seconds, with time steps of 0.04, 0.02, and 0.01 seconds. Figure 19 shows the data, simulation results for a time step of 0.04 sec, and simulation results for a time step of 0.01 sec.



**Figure 19. Time Step Study Profiles. Rows: Favre-averaged Vertical Velocity, Horizontal Velocity, Density, and Turbulent Kinetic Energy Columns: (a) Data (b) time step = 0.04 sec, and (c) time step = 0.01 sec, Mesh = 500K,  $\tau_{\text{filter}} = 0.08$  sec**

Comparing the simulation results with the data in Figure 19, it is clear that there are significant discrepancies. It was chosen, for computational cost purposes, to use the larger filter width of 0.08 seconds compared to the 0.02 seconds used in the mesh refinement study, as well as the medium grid (500K). Both the relatively low mesh density and the relatively high filter width, imply that the dynamics are somewhat limited. Movies of the simulation results support this assertion showing the symmetric puffing mode but no secondary asymmetries.

With the higher frequencies damped, it is expected that the time step refinement study at the fixed filter width will be insensitive to the time step. Comparing the 0.04 second time step data with the 0.01 second time step data in Figure 19 indicates that the simulation results are relatively insensitive to time step. In this regard, the results are highly desirable.

### ***Quantifying the Uncertainties***

Up to this point qualitative comparisons have been made. For validation purposes, it is necessary to quantify the uncertainty. To achieve this goal, it is necessary to select a validation metric. For this study, the centerline vertical velocity profile has been selected as the measure of interest, as shown in Figure 20, for the four mesh densities. This one-dimensional metric is a compromise between a global point measure and a two-dimensional measure.

The vertical velocity profile captures the dominant physical trends including the collapse of the vapor dome and acceleration of the plume. As noted in the mesh refinement study, it is perhaps not as sensitive to small scale mixing as is the centerline density. Relative to the fire application, capturing the centerline velocity profile is indicative of an ability to capture the overall buoyancy in the flow.

To make the comparison quantitative we use a statistical metric (Oberkampf and Barone, 2004). The statistical test uses the mean difference between the data and the simulation results as a function (in this case) of the vertical distance from the plume source. The simulation results for the 2 million node simulation, the data, and the 95% confidence interval for the data are shown in Figure 21. The metric uses the 95% confidence intervals about the data to establish where the “truth” lies, and the mean difference is expressed relative to this confidence interval. Graphically the result is shown in Figure 22.

The fact that the simulation results are within the confidence interval of the data above an elevation of 0.4 m is very encouraging. Even the excursion from the data at lower elevations, while outside the confidence interval of the data, is not more than twice the confidence interval. However, the mesh refinement study did not show grid insensitivity between the 2M node solution shown and the next coarsest grid at 1M node. Further, the scalar data would show a larger discrepancy between the simulation and the data, as it appears to be more sensitive to small scale mixing features.

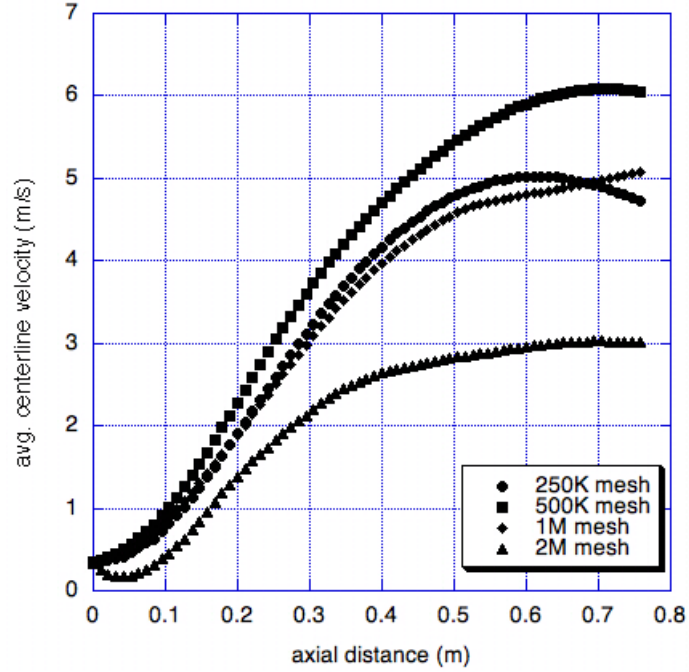


Figure 20. Centerline Vertical Velocity for the Four Mesh Densities Studied.

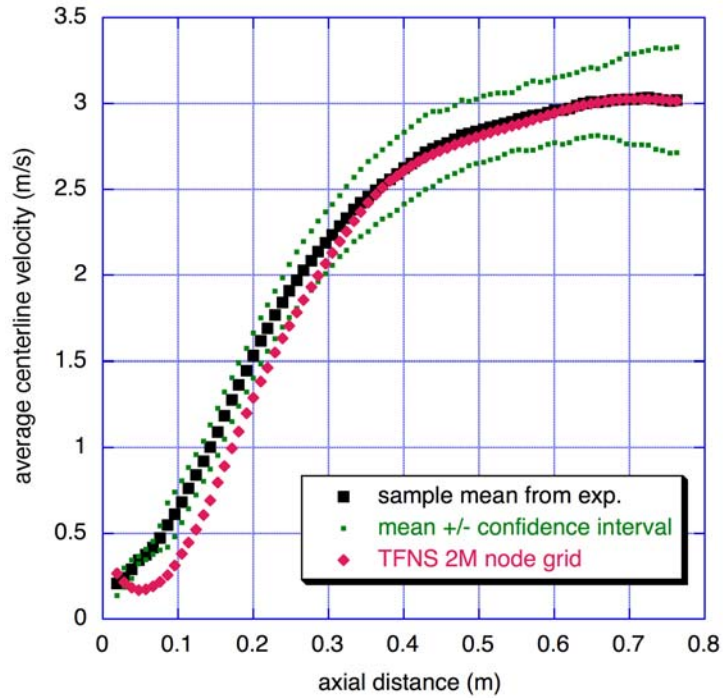
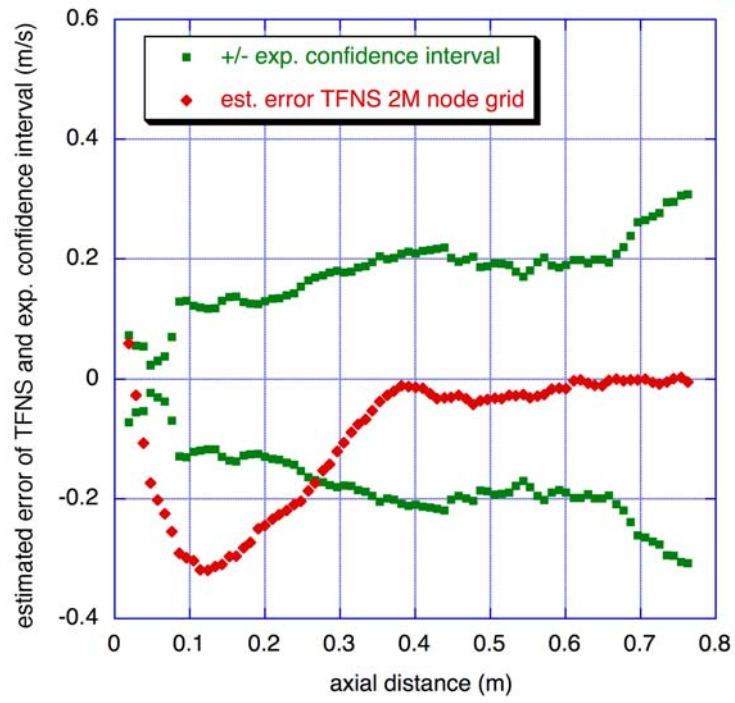


Figure 21. Centerline Vertical Velocity Data and 2M Node TFNS Simulation



**Figure 22. Experimental Confidence Interval and Estimated Error of 2M TFNS Simulation**

## Discussion

The mesh sensitivity of the results warrants further discussion, in particular the role of buoyancy generated turbulence. Further, additional discussion as to the implication of these results to heat transfer in a fire is also warranted.

### ***Dynamics of Buoyant Turbulence***

After the completion of this study but before its final publication, one of the authors, Sheldon Tieszen, spent time at the 2004 Stanford Center for Turbulence Research Summer Program. Comparing the experimental data with high resolution LES in discussion with a Rayleigh-Taylor (RT) expert, yielded valuable insight into the dynamic nature of the turbulence (Tieszen, et al., 2004). In particular two dynamical modes were noted. The first is driven by the classical RT instability as the helium emanates from the source into the overlying relatively heavy air. A classical bubble and spike structure forms with helium bubbles and air spikes. The resulting mixing produces a more homogeneous helium/air mixture that has a relatively sharp horizontal density gradient between the mixture and the surrounding air at the edge of the plume source.

The second mode is the rollup of the large vortex that is characteristic of puffing. The misalignment of the horizontal gradient with the vertical hydrostatic field results in the edge vortex that eventually grows to the centerline as it is advected upward. The velocity field resulting from this vortex results in air entrainment deep into the plume, over the top of the emanating helium, thus creating the conditions for the classical RT instability to start again. The air spikes formed in the RT phase penetrate downward all the way to the plume source. The large vortex sweeps the air into the plume centerline, thus changing the time-mean density of the plume centerline. The higher density of the air/helium mix results in a lower centerline vertical velocity than would be present if no air had penetrated to the centerline.

The presence of the two distinct triggering phenomena can explain the mesh sensitivity of the results obtained in the last section. As noted in Tieszen, et al., 2004, the bubble and spike structure has a much higher spatial frequency than the instability triggered at the plume edge. A much higher mesh density is required to capture the thin air spikes than the edge instability. If the air spikes are not captured, the mean plume centerline density will be too low compared to the data (compare Figures 9 and 16), and the centerline vertical velocity will be too high (compare Figures 7 and 13). Figure 14 shows that for the 2 million node mesh, the air spikes penetrate into the centerline. For the 250K and 500K node meshes, no air spikes are even formed. In the 1 million node mesh, spikes are formed but are advected downstream before they have a chance to penetrate deeply into the centerline. Both the RT mode and the vortex rollup are important to mixing dynamics. The roll up can be captured with relatively coarse meshes, but the RT spike structure requires much finer meshes to resolve.

## ***Buoyant Vorticity Generation***

The study discussed to this point validated the use of the standard k- $\epsilon$  model as a TFNS closure (Eq. 10 & 11, with  $C_{BVG}$  and  $C_{\epsilon 3}$  set to zero). Nicolette, et al., 2004 have proposed modifications to the standard k- $\epsilon$  model to account for buoyancy produced turbulence resulting from hydrostatic and hydrodynamic vorticity generation mechanisms. An additional turbulent kinetic energy production term in the turbulent kinetic energy equation was identified and modeled. The model was calibrated ( $C_{BVG}$  and  $C_{\epsilon 3}$  set to 0.35 and zero, in Eq. 10 & 11 respectively) in the context of eddy viscosity models, i.e., turbulent mixing in the long time-averaged sense can be represented by a diffusion term with a turbulent viscosity.

The form of the buoyant production term chosen is physically consistent with the shear production term. In both cases, the eddy viscosity is used as a prefactor to the term. In the context of TFNS, this eddy viscosity is a function of the temporal filter width. The physical meaning is the same as shear production. As the filter width goes to zero, the production approaches zero and as the filter width goes to infinity, the production approaches the RANS limit. The BVG production term uses the time-mean density gradients analogous to the time-mean velocity gradients in the shear production term.

Figure 23 shows a comparison between the standard and BVG modified k- $\epsilon$  model for two different mesh levels, 250K and 1 M node meshes for a temporal filter width of 0.02 seconds and a time step of 0.01 seconds. The instantaneous density plots in Figure 23 are indicative of phenomena observed in movies of the flow dynamics. As noted before with the standard k- $\epsilon$  model, there were significant differences in dynamics between the 250K and 1M node meshes. With the BVG model, both mesh densities produced essentially symmetric mode puffing. However, the BVG model appeared to dampen the amplitude of the puffs as may be expected from a higher viscosity model. Further, there was no evidence of smaller scale asymmetric features in the results of the 1 M node mesh with BVG.

Figures 24 – 27 show similar comparisons between the standard and BVG modified k- $\epsilon$  model, but for the Favre-averaged vertical velocity profile, the Favre-averaged horizontal velocity profile, the time-averaged density profile, and the Favre-averaged turbulent kinetic energy profile, respectively. On the positive side, the BVG results show somewhat less mesh sensitivity than the standard model. On the negative side, the effect of the increased eddy viscosity is to dampen the flow, which results in poorer overall comparisons with the data. The bottom line is that in theory the BVG modification should produce a better model, but in practice for TFNS applications it does not. The reason for the poor comparisons is a basic incompatibility between the need to minimize viscosity to produce low frequency dynamics and the desire to represent subfilter turbulence as a viscosity.

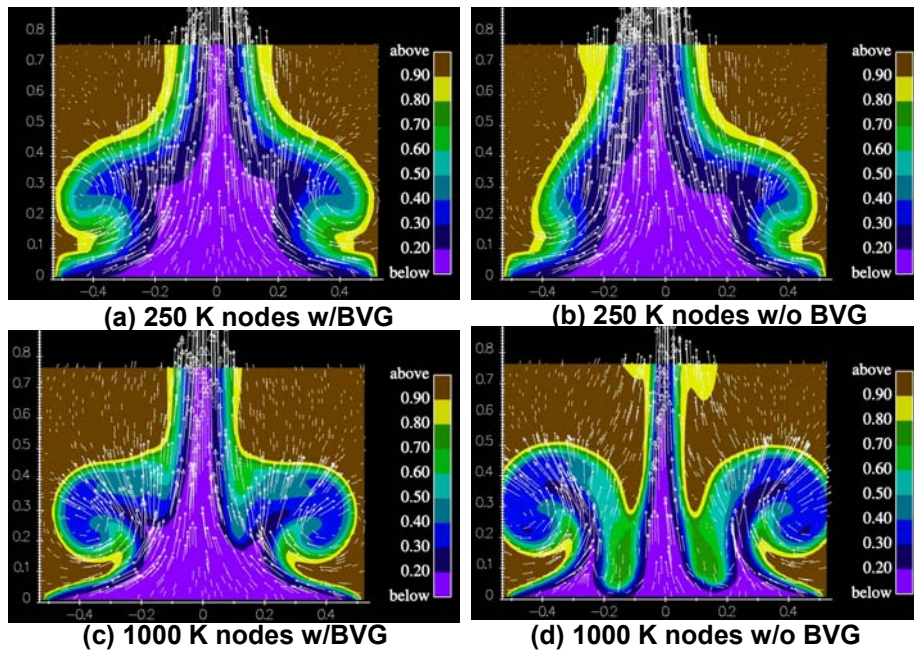


Figure 23. Model Comparison for Instantaneous Density Profiles ( $\text{kg/m}^3$ )  
 (a) w/BVG 250K (b) w/o BVG 250K (c) w/BVG 1M and (d) w/o BVG 1M node mesh

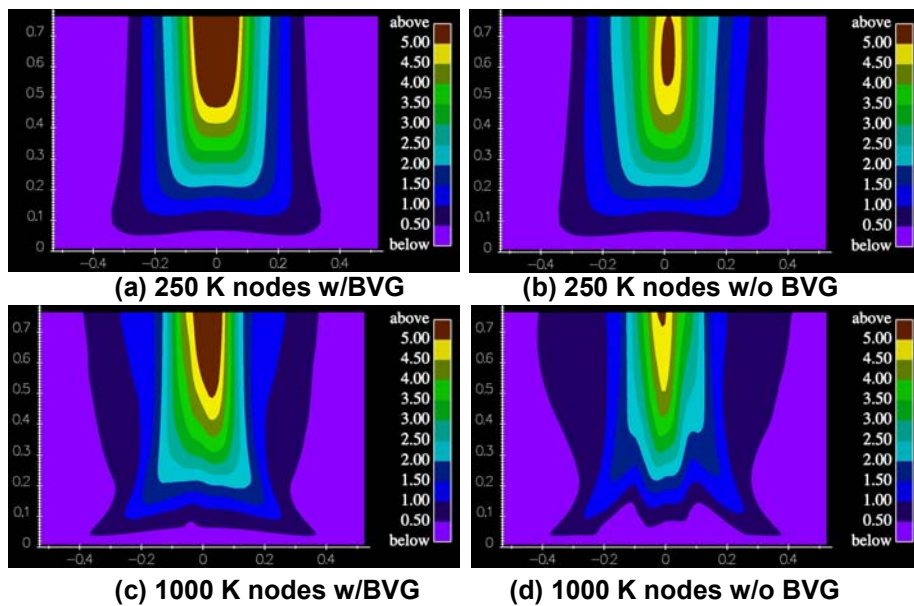


Figure 24. Model Comparison for Favre-averaged Vertical Velocity Profiles ( $\text{m/s}$ ).  
 (a) w/BVG 250K (b) w/o BVG 250K (c) w/BVG 1M and (d) w/o BVG 1M node mesh

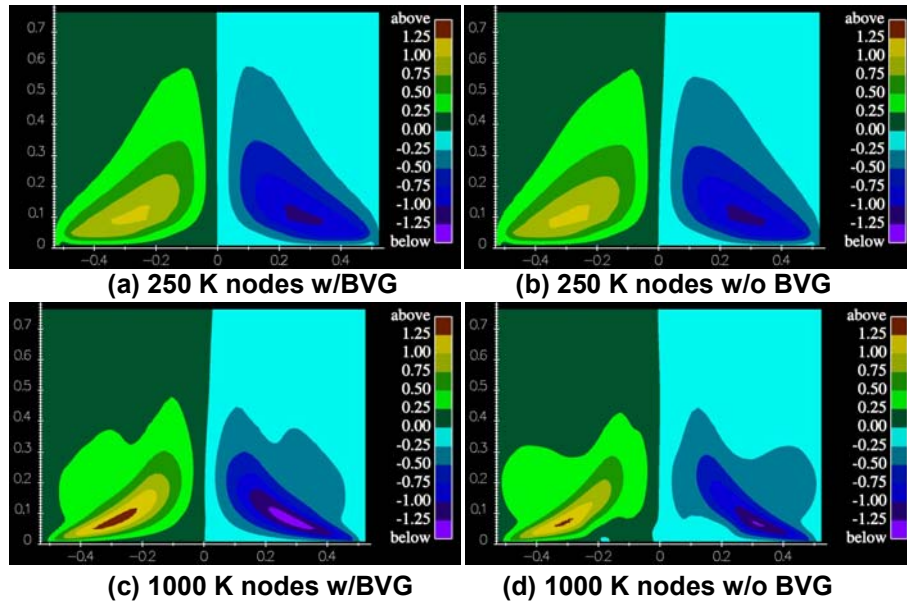


Figure 25. Model Comparison for Favre-averaged Horizontal Velocity Profiles (m/s).  
 (a) w/BVG 250K (b) w/o BVG 250K (c) w/BVG 1M and (d) w/o BVG 1M node mesh

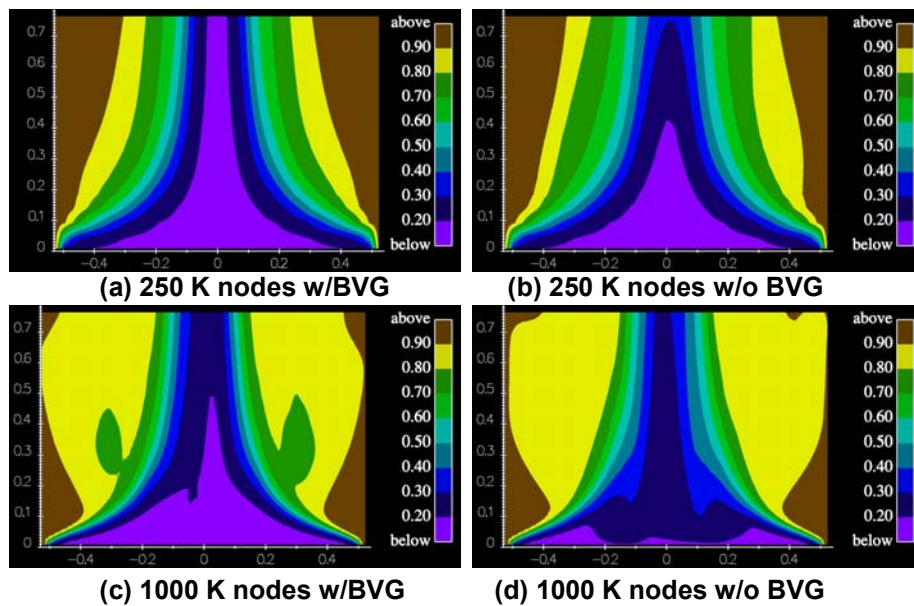
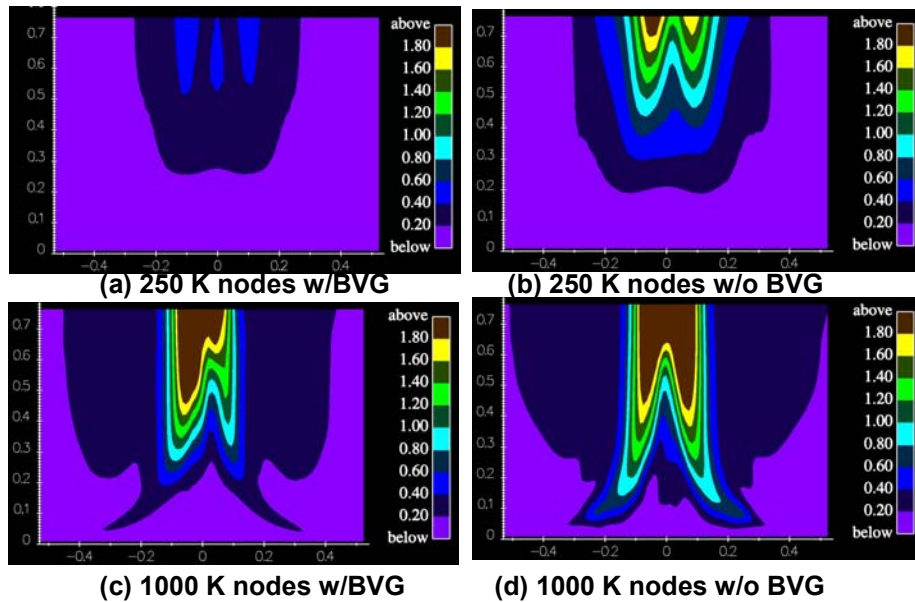


Figure 26. Model Comparison for Time-averaged Density Profiles ( $\text{kg/m}^3$ ).  
 (a) w/BVG 250K (b) w/o BVG 250K (c) w/BVG 1M and (d) w/o BVG 1M node mesh



**Figure 27. Model Comparison for Favre-averaged Turbulent Kinetic Energy Profiles ( $\text{m}^2/\text{s}^2$ ).  
 (a) w/BVG 250K (b) w/o BVG 250K (c) w/BVG 1M and (d) w/o BVG 1M node mesh**

Since the BVG model uses the time-mean density gradients, it cannot represent physical processes that have no gradient in the mean. Hence, it can capture the effect of the roll up of the large vortex because there is a persistent, time-mean edge to the plume. However, for the RT structures, there is no persistent bubble or spike over time. Thus this model cannot capture that level of physics fidelity. However from an engineering perspective, in the RANS limit, Nicolette, et al., 2004 show that the BVG model produces reasonable behavior. The upper row of symbols in the simulation matrix, Figure 11, refers to results presented in Nicolette, et al., 2004. The reader is referred to that study to understand quantitative comparisons of the data in the RANS limit.

By design of the TFNS, the BVG modification will also go to zero in the limit of zero temporal filter width. However, as indicated in Figures 24 through 27, in between good behavior in the RANS and DNS limit, the damping produced by the increased viscosity of the BVG model is counterproductive, except in a somewhat decreased mesh dependency of the results.

Clearly in the limiting cases of infinite and vanishing temporal filter width the model will give very different dynamical behavior. A limited study was done by varying the filter width between 0.08 second and 0.02 seconds (i.e., nominally 1/9 the puffing frequency and 1/36 the puffing frequency) with the time step held at 0.01 second. The results are shown in Figure 28. Somewhat surprisingly, there is very little difference in the averaged results for this factor of four change in filter width for the 500K mesh chosen.

The expected result is that the reduced filter width will permit more dynamics and thus result in a better prediction. The fact that this result was not obtained with the 500K mesh suggests that the change in model viscosity due to the change in filter did not change the dynamics. Another “viscosity” in the problem is numerical viscosity. Numerical viscosity is a function of the numerical schemes used and the spatial discretization. The 500K mesh results suggest for the second order upwind scheme used and the 500K mesh, that the model viscosity is less than the numerical viscosity. Due to a lack of computational resources, the authors did not pursue a temporal refinement study on the 1M and 2M node meshes.

It should also be noted that throughout this study, other than the temporal filter width refinement study on the 500 K mesh, the ratio of the filter width to time step was held at 2. This is the minimum value to assure that there is no aliasing. It is not necessarily the “correct” value. Discussions with Dave Pruett of James Madison University (Pruett, private communication, 2004) suggest that the temporal filter should perhaps be a factor of 4 times the time step to correctly capture the eddy viscosity in the limit as DNS is approached. However, for the current study, clearly the low order numerics and coarse meshes relative to the physics, suggest that the overall viscosity (numerical + model) is sufficiently high that it is not possible to test this premise in this study. Clearly, more work is needed to fully understand the interaction of numerics, mesh-density and filter width.

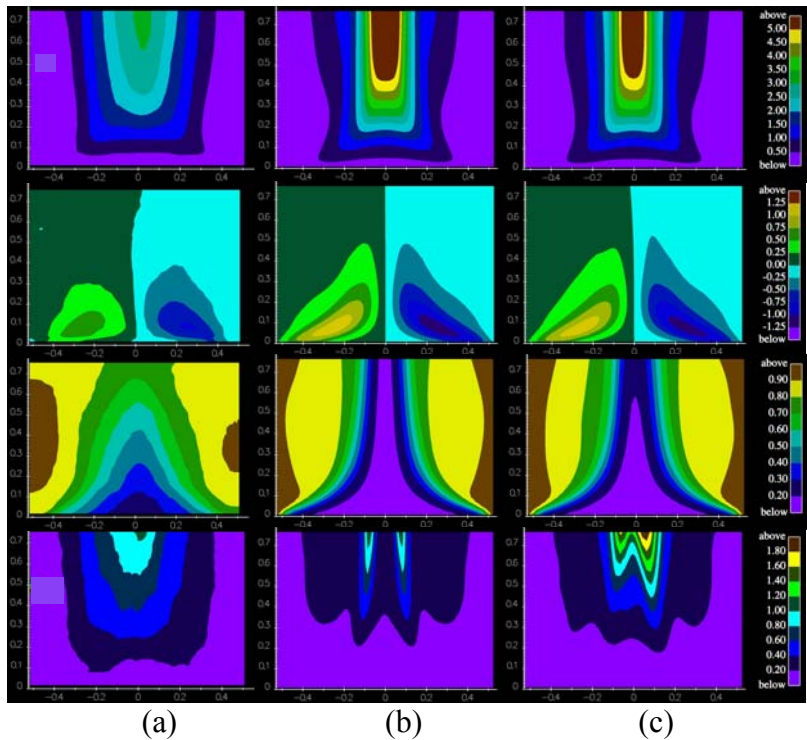


Figure 28. Temporal Filter Study Profiles. Rows: Favre-averaged Vertical Velocity, Horizontal Velocity, Density, and Turbulent Kinetic Energy. Columns: (a) Data (b)  $\tau_{\text{filter}} = 0.08$  sec, and (c)  $\tau_{\text{filter}} = 0.02$  sec, Mesh = 500K,  $\Delta t = 0.01$  sec,

## ***Toward Effects on Heat Transfer***

The primary purpose for conducting this study is to quantify the uncertainties in using TFNS with the proposed closure model for fire environments. This study is one of several planned validation studies with flows of increasing complexity leading to validation studies in fire environments of relevance. By using a validation suite beginning with the least complex flow; it is possible to untangle the sources of the uncertainty. Certainly in this case, the role of buoyant vorticity generation is complex enough without being coupled to the complexities of turbulent combustion, soot generation, radiation, and wall production of turbulence.

However, having established the degree to which we can model the effects of buoyant turbulence in the absence of surfaces, future studies can focus on these further complexities, in particular, the effects of turbulence on convective and radiative heat transfer. Turbulence, and hence turbulence models, are intricately linked with heat transfer through both convective and radiative effects. The physics of convection is such that the full range of turbulence length scale is involved in convection. Typically in the near wall region of an object, the length scale of the dominant turbulent structures increases in proportion to the distance from the wall. For a given convective velocity, the transit period of these structures also increases with increasing distance from the wall. Thus the highest frequencies are nearest the wall.

By temporally filtering the Navier-Stokes equations, the high frequency, near wall fluctuations are filtered out of the mean flow equations except through the modeled terms. Thus, it is necessary to model the flows in the near wall region. In the long time-averaged limit, the modeling limits to standard RANS wall treatments, like law of the wall, low Reynolds number models, two-layer treatments, or the  $v2f$  model of Durbin and colleagues (Durbin, et. al, 2001). One of the key advantages of temporal filtering is that it can directly utilize the extensive effort that has gone into RANS near wall models. One of the key limitations that has prevented wide spread use of spatial filtering (LES) is that the near wall region requires near DNS level grids in order for the filtering to capture the “large eddies”. With the current filtering, the “large eddies” in the near wall region have sufficiently high frequencies that they are naturally filtered out and modeled as high frequency fluctuations. In the limit of a near ergodic flow (low frequency forcing), it can be expected that the near wall will be stationary, and RANS-like boundary conditions will apply. This argument is not meant to imply that RANS boundary condition treatments are perfect, or even of particularly high quality, just that they are applicable and extensive effort has gone into their development and characterization.

It is beyond the goal of this current study to validate a near wall treatment for convection. Evans, et al., 2004, has recently conducted such a study with standard law of the wall and the  $v2f$  model using the standard eddy viscosity definition. However, as part of the current study, it is of interest to demonstrate that RANS wall treatments can be used with the TFNS formulation. To this end, the natural convection problem described in Evans et al., 2004 was run with a narrow temporal filter width of 0.004 seconds (time step = 0.002 sec) using the  $v2f$  wall treatment. Using the same mesh as in the Evans, et al., 2004 study for the  $v2f$  model resulted in a steady solution even though the grid spacing at the wall

was sufficient to produce a  $y^+$  of near unity. The  $v2f$  model requires meshing down to the surface in the wall normal direction, but permits relatively coarse meshing in the two transverse directions. The result is a high aspect ratio mesh in the near wall region. With this type of mesh, even with the very narrow filter width of 0.004 seconds, the flow was steady as desired (since there was no low frequency external forcing as in the helium plume).

However, it is a legitimate question to ask whether this result was due to mesh resolution or a model inadequacy. In order to achieve high mesh density, a two-dimensional problem was run with the same wall normal mesh spacing, but much tighter spacing in the flow direction. For a temporal filter width of 0.004 seconds (time step = 0.002 sec), strong dynamics was achieved in the boundary layer. Figure 29 shows a segment of the solution in the near wall region with clear indication of buoyant eddy structures. In the limit of vanishing filter width, the eddy viscosity will vanish, and theoretically the solution should tend toward the Navier-Stokes limit if there is the proper mesh density to reflect the dynamics. In practical fire problems, this mesh density will not likely be achievable even with the largest planned computational machines.

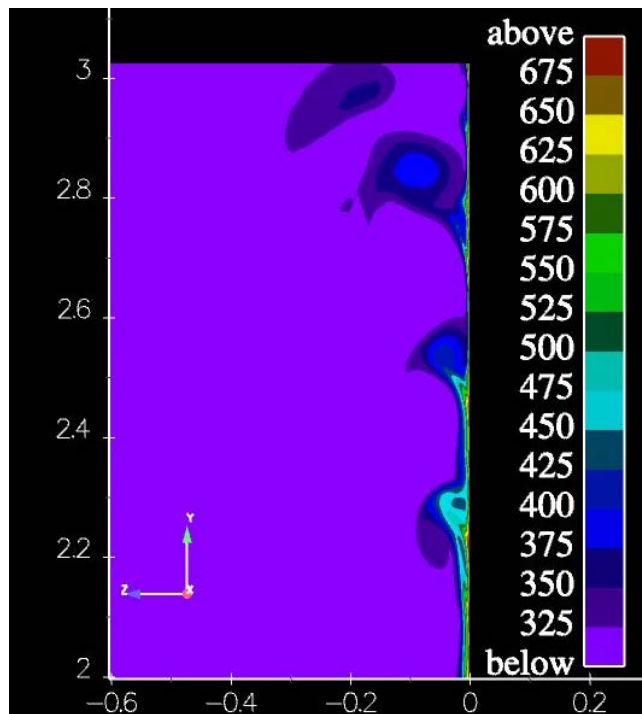


**Figure 29. Two Dimensional Natural Convection Simulation for the Conditions of Evans, et al., 2004.  $\tau_{\text{filter}} = 0.004$  seconds (time step = 0.002 seconds) results in strong dynamics with an 800 x 135 mesh. Temperature is plotted.**

Regarding TFNS and radiation heat transfer, the principal theoretical advantage of TFNS over RANS is that subfilter process models will be given more temporally relevant information from the solution of the filtered Navier Stokes equations. Radiation is itself a

highly non-linear process, but it arises in fires from soot, the formation of which is also a highly non-linear process. It is very often the case that the time-averaged output of a highly non-linear process is not generally well correlated with time-averaged inputs. For example, the hottest part of a fire is where combustion is occurring most frequently. For fires, this location is where the highest spatial frequency of stoichiometric surfaces occur. In a RANS model, the mean will be stoichiometric and fluctuations must be passed as low order moments (such as turbulent kinetic energy) or other information (such as turbulent kinetic energy dissipation, or scalar dissipation).

In reality, the locations with the highest spatial frequency of stoichiometric surfaces also have the highest intermittency in all variables. It is where the fuel is meeting the air. Thus the physics of the problem is dominated by the intermittency, not the mean value being stoichiometric in this region. The benefit of TFNS is that up to the level permitted by the grid and the temporal filter, at least low frequency (typically large amplitude), intermittency can be accounted for by the flow solution, and thus, the low order fluctuating moments that are passed to the subfilter models better represent the actual intermittency. This feature should result in more accurate time-averaged predictions, the validation of which will be the subject of a future study.

## Conclusions

A simple closure model for the temporally filtered Navier-Stokes (TFNS) equations has been developed and validated against a helium data set. At high mesh densities (2 million nodes), the model performs well as evidenced by a statistical validation metric, which shows that the simulated centerline vertical velocity falls within the 95% confidence interval of the data for elevations above 0.4 m, and the discrepancy is never greater than twice the confidence interval. The model exhibits mesh spacing sensitivity in spite of the filter width being temporal and fixed for the simulations. Use of a submodel for buoyant vorticity generation resulted in significantly less mesh spacing sensitivity, but also overall significantly poorer predictive performance. There were small sensitivities to time step (expected) and temporal filter width (not expected) for the medium mesh density chosen. Future studies will use the developed turbulence model in flows of increasing complexity to build confidence and to determine the uncertainties in predicting heat transfer in fires.

## References

- Boughton, B. D., Tieszen, S. R., Gill, W., Romero, V. J., Sobolik, K. B., "Integrated Modeling and Simulation Validation Plan for the W80-3 Abnormal Thermal Environment Qualification – Version 1.0," Sandia National Laboratories, Albuquerque, NM, SAND2003-4152, November 2003 (Official Use Only).
- Deardorff, J. W., 1980, "Stratocumulus-Capped Mixed Layers Derived From a Three-Dimensional Model," *Boundary Layer Meteorology*, 18:495-527.
- DesJardin, P. E., O'Hern, T. J., and Tieszen, S. R., 2004, "Large Eddy Simulation and Experimental Measurements of the Near-Field of a Large Turbulent Helium Plume," *Physics of Fluids*, Vol 16, no. 6, pp 1866-1883.
- Durbin, P. A., Pettersson Reif, B. A., 2001, *Statistical Theory and Modeling for Turbulent Flows*, John Wiley & Sons, New York, NY.
- Evans, G., Greif, R., Siebers, D., and Tieszen, S., 2004, "Turbulent Mixed Convection from a Large, High Temperature Vertical Flat Surface," (In review).
- Girimaji, S. S., Srinivasan, R., Jeong, E., 2003, "PANS Turbulence Model for Seamless Transition Between RANS and LES: Fixed-Point Analysis and Preliminary Results," *Proceedings of ASME FEDSM'03*, July 13-16, Honolulu, Hawaii, pp. 1-9.
- Hirsh, C., 1990, *Numerical Computation of Internal and External Flows*, Volume 2. John Wiley & Sons, New York, NY.
- Moen, C. D., Evans, G. H., Domino, S. P., and Burns, S. P., 2002, "A Multi-Mechanics Approach to Computational Heat Transfer", 2002 ASME International Mechanical Engineering Congress and Exhibition, November 17-22, New Orleans, LA, USA.
- Nicolette, V. F., Tieszen, S. R., Black, A. R., Domino, S. P. and O'Hern, T. J., 2004, "A Buoyant Vorticity Generation Model of Turbulence for Buoyant Flows," (In preparation.)
- Oberkampf, W. L., and Barone, M. F., 2004, "Measurement of Agreement Between Computation and Experiment: Validation Metrics," 34<sup>th</sup> AIAA Fluid Dynamics Conference, Portland, Oregon, June 28-July 1, Paper No 2004-2626.
- O'Hern, T. J., Weckman, E. J., Gerhart, A. L., Tieszen, S. R., and Schefer, R. W., 2004, "Experimental Study of a Turbulent Buoyant Helium Plume," (In preparation.)

- Pruett, C. D., 2000, "Eulerian Time-Domain Filtering for Spatial Large-Eddy Simulation," *AIAA Journal*, 38:1634-1642.
- Pruett, C. D., Gatski, T. B., Grosch, C. E., Thacker, W. D., 2003, "The Temporally Filtered Navier-Stokes Equations: Properties of the Residual Stress," *Physics of Fluids*, 15:2127-2140.
- Spalart, P. R., "Strategies for Turbulence Modeling and Simulations," 4<sup>th</sup> International Symposium on Engineering Turbulence Modeling and Measurements, May 24-26, Corsica, France.
- Tieszen, S. R., Chu, T. Y., Dobranich, D., Romero, V. J., Trucano, T. G., Nakos, J. T., Moffatt, W. C., Hendrickson, T. F., Sobolik, K. B., Kempka, S. N., Pilch, M., 2002, "Integrated Modeling and Simulation Validation Plan for the W76-1 Abnormal Thermal Environment Qualification –Version 1.0," Sandia National Laboratories, Albuquerque, NM, SAND2002-1740 (Official Use Only).
- Tieszen, S. R., Pitsch, H., Blanquart, G., and Abarzhi, S., 2004, "Toward the development of a LES\_SGS closure model for buoyant plumes," *Proceedings of the Summer Program 2004*, Center for Turbulence Research, Stanford University, Stanford, CA, pp. 341-352.
- Tennekes, H. and Lumley, J. L., 1972, *A First Course in Turbulence*, The MIT Press, Cambridge, Mass.
- Tieszen, S. R., Black, A. R., Moen, C. D., Chu, T. Y., Nicolette, V. F., Gill, W., Burns, S. P., Moffatt, W. C., 2001, "SIERRA/FUEGO and SIERRA/SYRINX Verification and Validation Plan Version 2.0," Sandia National Laboratories, Albuquerque, NM, SAND2001-3798 (Official Use Only).

## **Distribution**

### **External**

Department of Energy  
Attn: K. Greenaugh, NA-115.3  
1000 Independence Ave., SW  
Washington, DC 20585

James Madison University  
Attn: Prof. C. David Pruett  
MSC 7803  
18 Burruss Hall  
Harrisonburg, VA 22807

State University of New York, Buffalo  
Attn: Prof. Paul DesJardin  
Mechanical and Aerospace Engineering  
State University of New York at Buffalo  
Buffalo, NY 14260

Computational Industrial Technologies (2)  
Attn: Dr. Bjorn Magnussen  
Dr. Bjorn Erling Vembe  
Computational Industry Technologies AS  
P.O Box 1275, Pirsenteret  
N-7462 Trondheim  
Norway

Imperial College of Science, Technology and Medicine  
Attn: Prof. Bill Jones  
Department of Chemical Engineering and Chemical Technology  
Prince Consort Road  
London SW7 2BY  
United Kingdom

University of Utah (3)  
Attn: Prof. Philip Smith  
Prof. Adel Sarofim  
Prof. Eric Eddings  
University of Utah  
Department of Chemical Engineering  
50 S Central Campus Dr.  
Merrill Engineering Building Rm 3290  
Salt Lake City, Utah 84112-9203

Stanford University (3)  
Attn: Prof. Heinz Pitsch  
Dr. Frank Ham  
Dr. Gianlucca Iaccarino

Blg. 500  
440 Escondido Mall  
Stanford, CA 94305-3030

Purdue University  
Attn: J. P. Gore  
Engineering Administration Building, Room 101  
400 Centennial Mail Drive  
West Lafayette, IN 47907-2016

University of Maryland  
Attn: Prof. Arnaud Trouvé  
Department of Fire Protection Engineering  
0151 Glenn L. Martin Hall  
College Park, MD 20742-3031 (USA)

## Internal

1	MS-0139	09904	R. K. Thomas
1	MS-0139	09905	S. E. Lott
1	MS-0316	09233	J. N. Shadid
1	MS-0316	09233	R. C. Schmidt
1	MS-0316	09233	T. M. Smith
1	MS-0382	09141	S. P. Domino
1	MS-0382	09141	E. A. Boucheron
1	MS-0384	09100	C. W. Peterson
1	MS-0481	02114	T. F. Hendrickson
1	MS-0481	02132	S. E. Slezak
1	MS-0481	02114	M. A. Rosenthal
1	MS-0819	09211	T. G. Trucano
1	MS-0824	09130	T. Y. Chu
1	MS-0825	09110	W. L. Hermina
1	MS-0828	09133	A. R. Black
1	MS-0828	09133	K. J. Dowding
1	MS-0828	09133	W. L. Oberkampf
1	MS-0828	09133	M. Pilch
1	MS-0828	09133	V. J. Romero
1	MS-0834	09112	K. L. Erickson
1	MS-0834	09112	S. P. Kearney
1	MS-0834	09112	T. J. O'Hern
1	MS-0834	09114	J. E. Johannes
1	MS-0834	09114	H. K. Moffat

1	MS-0836	09116	E. S. Hertel
1	MS-0836	09116	B. D. Boughton
1	MS-0836	09116	D. Dobranich
1	MS-0836	09116	R. E. Hogan
1	MS-0836	09132	C. Romero
1	MS-0836	09132	W. Gill
1	MS-0847	09120	P. J. Wilson
1	MS-0836	09132	A. L. Brown
1	MS-0836	09132	V. G. Figueroa
1	MS-0836	09132	W. D. Sundberg
1	MS-0836	09132	J. Suo-Anttila
5	MS-1135	09132	L. A. Gritz
15	MS-1135	09132	S. R. Tieszen
1	MS-1135	09132	V. F. Nicolette
1	MS-1135	09134	S. Heffelfinger
1	MS-1139	09132	T. K. Blanchat
1	MS-9042	08775	C. D. Moen
1	MS-9042	08775	G. H. Evans
1	MS-9042	08775	G. J. Wagner
1	MS-9051	08351	A. R. Kerstein
1	MS-9051	08367	J. C. Oefelein
1	MS-9051	08367	R. W. Schefer
1	MS-9052	08367	J. O. Keller
1	MS-9950	08775	G. M. Laskowski
2	MS-0899	09616	Technical Library
1	MS-9018	08945-1	Central Technical Files